

**Impacts of Cloud Microphysics Parameterizations on Simulated Aerosol-Cloud-Interactions
for Deep Convective Clouds over Houston**

Yuwei Zhang^{1,2}, Jiwen Fan^{2,*}, Zhanqing Li¹, Daniel Rosenfeld³

¹Department of Atmospheric and Oceanic Science, University of Maryland, College Park, MD,
USA

²Atmospheric Sciences and Global Change Division, Pacific Northwest National Laboratory,
Richland, WA, USA

³ Institute of Earth Sciences, The Hebrew University of Jerusalem, Jerusalem, Israel

* *Correspondence to:* Jiwen Fan (jiwen.fan@pnnl.gov)

Abstract

Aerosol-cloud interactions remain largely uncertain in predicting their impacts on weather and climate. Cloud microphysics parameterization is one of the factors leading to the large uncertainty. Here we investigate the impacts of anthropogenic aerosols on the convective intensity and precipitation of a thunderstorm occurring on 19 June 2013 over Houston with the Chemistry version of Weather Research and Forecast model (WRF-Chem) using the Morrison two-moment bulk scheme and spectral-bin microphysics (SBM) scheme. We find that the SBM predicts a deep convective cloud agreeing better with observations in terms of reflectivity and precipitation compared with the Morrison bulk scheme that has been used in many weather and climate models. With the SBM scheme, we see a significant invigoration effect on convective intensity and precipitation by anthropogenic aerosols mainly through enhanced condensation latent heating. Whereas such an effect is absent with the Morrison two-moment bulk microphysics, mainly because the saturation adjustment approach for droplet condensation and evaporation calculation limits the enhancement in (1) condensation latent heat by removing the dependence of condensation on droplet properties and (2) in ice-related processes by a more efficient conversion of droplets into raindrops, which leads to fewer cloud droplets being transported to the altitudes above the freezing level.

1 Introduction

Deep convective clouds (DCCs) produce copious precipitation and play important roles in the hydrological and energy cycle as well as regional and global circulation (e.g., Arakawa, 2004; Houze, 2014). DCCs and associated precipitation are determined by water vapor, vertical motion of air, and cloud microphysics that could be affected by aerosols through aerosol-radiative interactions (ARI) or aerosol-cloud interactions (ACI) or both. The cloud-mediated aerosol effects are recognized by the Intergovernmental Panel on Climate Change (IPCC) as one of the key sources of uncertainty in our knowledge of Earth's energy budget and anthropogenic climate forcing (e.g., Arakawa, 2004; Andreae et al., 2005; Haywood and Boucher, 2000; Lohmann and Feichter, 2005).

Precipitation, latent heat, and cloud radiative forcing associated with DCCs are strongly associated with cloud microphysical processes, which can be modulated by aerosols through serving as cloud condensation nuclei (CCN) and ice nuclei (IN). For aerosol-DCC interactions, a well-known theory is that increasing aerosol concentrations can suppress warm rain as a result of increased droplet numbers but reduced droplet size. This allows more cloud droplets to be lifted to altitudes above the freezing level, inducing stronger ice microphysical processes (e.g., droplet freezing, riming, and deposition) which release larger latent heating, thereby invigorating convective updrafts (referred to as “cold-phase invigoration,”; Khain et al. 2005; Rosenfeld et al., 2008). It is significant in the situations of warm-cloud bases ($> 15^{\circ}\text{C}$; Fan et al., 2012b; Li et al., 2011; Rosenfeld et al., 2014; Tao and Li, 2016) and weak wind shear (Fan et al., 2009, 2012b, 2013; Li et al., 2008; Lebo et al., 2012). Grabowski and Morrison (2016; 2020) rejected this invigoration concept by arguing that the increase in the buoyancy by freezing is completely offset by the buoyancy for carrying the extra cloud water across the freezing level. However, Rosenfeld

et al. (2008) showed that the buoyancy restores and increases after the precipitation of the ice hydrometeors that form upon freezing of the high supercooled liquid water content into large graupel and hail.

Another theory is that increasing aerosols enhances droplet nucleation particularly secondary nucleation after warm rain initiates, which promotes condensation because of larger integrated droplet surface area associated with a higher number of small droplets (Fan et al., 2007, 2013, 2018; Koren et al., 2014; Lebo, 2018; Sheffield et al., 2015; Chen et al., 2020). This so-called “warm-phase invigoration”, which is manifested in a warm, humid, and clean environment under which the addition of a large number of ultrafine aerosol particles from urban pollution leads to stronger invigoration than the “cold-phase invigoration” (Fan et al., 2018). Grabowski and Morrison (2020) proposed a different interpretation of the warm-phase invigoration from the literature listed above. They argued that condensation rates only depend on updraft velocity with the quasi-steady assumption (i.e., the true supersaturation is approximated with the equilibrium supersaturation), therefore they interpreted that it is the lower equilibrium supersaturation in polluted conditions that lead to a larger buoyancy, thus enhanced updraft speeds, and condensation. Several studies showed that the quasi-steady assumption is invalidated in the conditions of low droplet concentrations (Politovich and Cooper, 1988; Korolev and Mazin, 2003) or acceleration of vertical velocity (Pinsky et al., 2013).

Many factors can affect whether aerosols invigorate or suppress convective intensity through ACI, such as environmental wind shear (Fan et al., 2009; Lebo et al., 2012), relative humidity (Fan et al., 2007; Khain et al., 2008), and Convective Available Potential Energy (Lebo et al., 2012; Morrison, 2012; Storer et al., 2010). Meteorological buffering effects were also found for aerosol effects on convective clouds over a large region and long-time (over a few days and weeks)

simulations (Stevens and Feingold, 2009; van den Heever et al., 2011). Dagan et al. (2018) showed that the lifetimes of cloud systems are mostly much shorter than that and rarely reach this buffering state. For DCCs with complicated dynamics, thermodynamics, and microphysics, aerosol impacts are extremely complex and remain poorly known. Confidently isolating and quantifying an aerosol deep convective invigoration effect from observations requires very long-term measurements: data of 10 years are still not enough over the Southern Great Plains due to the large variability of meteorological conditions (Varble, 2018).

Modeling of ACI is quite dependent on cloud microphysics parameterization schemes (e.g., Fan et al., 2012a; Khain and Lynn, 2009; Khain et al., 2009, 2015; Lebo and Seinfeld, 2011; Lee et al., 2018; Loftus and Cotton, 2014; Wang et al., 2013). Two-moment bulk and bin schemes have been widely used in ACI studies (e.g., Chen et al., 2011; Fan et al., 2013; Khain et al., 2010). In two-moment bulk schemes, hydrometeor size distributions are diagnosed from the predicted number and mass with an assumed spectral shape (e.g., gamma function). The saturation adjustment approach is often used for calculating condensation and evaporation, meaning supersaturation and undersaturation with respect to water are removed in cloud within a timestep. Some bulk schemes take the explicit supersaturation approach to allow supersaturation to evolve (e.g., Morrison and Grabowski, 2007; 2008). In bin schemes, the size distributions of hydrometeors are discretized by a number of size bins and predicted, which represents some aerosol-cloud interaction processes more physically compared with bulk schemes (Fan et al., 2016; Khain et al., 2015). Supersaturation is generally predicted in bin schemes.

Many studies have shown that bulk schemes are limited in representing certain important microphysical processes such as aerosol activation, condensation, deposition, sedimentation, and rain evaporation (Ekman et al., 2011; Khain et al., 2009; Lee et al. 2018; Li et al., 2009; Milbrandt

and Yau, 2005; Morrison, 2012; Wang et al., 2013). Though bin cloud microphysics can provide a more rigorous numerical solution and a more robust cloud microphysics representation than typical bulk microphysics, it is often applied in simulations for process understanding but rarely in operational applications due to the expensive computation cost. For not introducing further computation cost, bins schemes are also often run with a prescribed aerosol spectrum assuming a fixed composition and a simple aerosol budget treatment without coupling with chemistry/aerosol calculations. As a result, many aerosol life cycle processes such as aerosol nucleation, growth, aqueous chemistry, aerosol resuspension, and below-cloud wet removal are missing or crudely parameterized. Therefore, it is difficult to simulate the spatial and temporal variabilities of aerosol chemical composition and size distribution. In Gao et al. (2016), we have coupled a spectral-bin microphysics scheme (SBM; Fan et al., 2012a; Khain et al., 2004) with the Chemistry version of Weather Research and Forecast model (WRF-Chem; Grell et al., 2005; Skamarock et al., 2008), called WRF-Chem-SBM, to address above-mentioned limitations. In this new model, the SBM was coupled with the Model for Simulating Aerosol Interactions and Chemistry (MOSAIC; Fast et al., 2006; Zaveri et al., 2008). The newly coupled system was initially evaluated for warm marine stratocumulus clouds and showed a much-improved simulation of cloud droplet number concentration and liquid water content compared with the default Morrison two-moment bulk scheme (Gao et al., 2016).

The Houston area in summer, where isolated convective clouds with very warm cloud-bases often occurred in the afternoon (Yuan et al., 2008), offers (a) a combination of polluted aerosols from the urban and industrial area of Houston with significantly low background aerosol concentrations surrounding Houston, (b) aerosol sources that are not correlated with meteorology, and (c) weak synoptic forcing along with strong local triggering in the form of land-sea contrasts

and sea breeze fronts. This combination allows the manifestation of potentially large aerosol effects. In this study, we choose a sea-breezed induced DCC case occurring 19-20 June 2013 near Houston to (1) evaluate the performances of WRF-Chem-SBM in simulating deep convective clouds and (2) gain a better understanding of the differences in aerosol effects predicted by SBM and the Morrison two-moment bulk scheme as well as the major factors/processes responsible for the differences. Considering that the convective clouds over the Houston area are mainly impacted by the aerosols produced from anthropogenic activities, we focus on the anthropogenic aerosol effect in this study. The simulated storm case is the same as the case for the Aerosol-Cloud-Precipitation-Cloud (ACPC) Model Intercomparison Project (Rosenfeld et al., 2014; www.acpcinitiative.org).

2 Case Description and Observational Data

The deep convective cloud event that we simulate in this study occurred on 19-20 June 2013 near Houston, Texas. The isolated relatively weak convective clouds started from the late morning because of a trailing front. With increased solar radiation in the early afternoon and strengthening of a sea breeze circulation that transports warm and humid air from the Gulf of Mexico to Houston urban area, deep convective cells over Houston and Galveston bay areas developed (Fig. 1). The strong convective cell observed near the Houston city was initiated around 2145 UTC (local time 16:45) and developed to its peak precipitation at 2217 UTC based on radar observation (Fig. 1). The maximum reflectivity was more than 55 dBZ. This storm cell lasted for about 1.5 hours.

We used the following observation data for model evaluation. Particulate matter (PM) 2.5 data provided by Texas Commission for Environmental Quality (TCEQ) at <https://www.tceq.texas.gov/agency/data/pm25.html> are used to evaluate the simulated aerosols near the surface. The data for evaluating cloud base heights and CCN number concentration at

cloud base are obtained from the Visible Infrared Imaging Radiometer Suite (VIIRS) retrievals based on the method of Rosenfeld et al., (2016). The 2-m temperature and 10-m winds are from the North American Land Data Assimilation System (NLDAS) with 0.125-deg resolution at <https://climatedataguide.ucar.edu/climate-data/nldas-north-american-land-data-assimilation-> system. The observed radar reflectivity is used to evaluate the simulated convective system. The radar reflectivity is obtained from Next-Generation Weather Radar (NEXRAD) network at <https://www.ncdc.noaa.gov/data-access/radar-data/nexrad-products>, with a temporal frequency of every ~ 5 minutes and 1 km horizontal spatial resolution.

3. Model description and experiments

We conducted model simulations using the version of WRF-Chem based on Gao et al. (2016) coupling with the Morrison two-moment scheme (Morrison et al., 2005; Morrison et al., 2009; Morrison and Milbrandt, 2011) and SBM (Khain et al., 2004; Fan et al., 2012). The version of SBM employed in this study is a fast version of the Hebrew University Cloud Model (HUCM) described by Khain et al. (2004) with improvements from Fan et al. (2012a) and (2017). The considered hydrometer size distributions are droplets/raindrops, cloud ice/snow, and graupel. The graupel version is used because it is more appropriate for simulating the convective storm over the Houston area than the hail version. SBM is currently coupled with the four-sector version of MOSAIC (0.039-0.156, 0.156-0.624, 0.624-2.5 and 2.5-10.0 μm). As detailed in Gao et al. (2016), the aerosol processes including aerosol activation, resuspension, and in-cloud wet-removal are also improved. Theoretically, both aerosol and cloud processes can be more realistically simulated particularly under the conditions of complicated aerosol compositions and aerosol spatial heterogeneity compared with original WRF-Chem. The dynamic core of WRF-Chem-SBM is the Advanced Research WRF model that is fully compressible and non-hydrostatic with a terrain-

following hydrostatic pressure vertical coordinate (Skamarock et al., 2008). The grid staggering is the Arakawa C-grid. The model uses the Runge-Kutta 3rd order time integration schemes, and the 3rd and 5th order advection schemes are selected for the vertical and horizontal directions, respectively. The positive-definite option is employed for the advection of moist and scalar variables.

Two nested domains with horizontal grid spacings of 2 and 0.5 km and horizontal grid points of 450×350 and 500×400 for Domain 1 and Domain 2, respectively, are used (Fig. 2a), with 51 vertical levels up to 50 hPa which allows about 50-100 m grid spacings below 2-km altitude and ~500 m above it. The simulations for Domain 1 and Domain 2 are run separately and the Domain 1 simulations serve to provide the chemical and aerosol lateral boundary and initial conditions of Domain 2. The chemical and aerosol lateral boundary and initial conditions for Domain 1 simulations were from a quasi-global WRF-Chem simulation at 1-degree grid spacing, and meteorological lateral boundary and initial conditions were created from MERRA-2 at the grid spacing of $0.5^\circ \times 0.625^\circ$ (Gelaro et al., 2017). Two simulations were run over Domain 1 with anthropogenic emissions turned on and off, respectively, to provide two different aerosol scenarios for the initial and boundary chemical and aerosol conditions for Domain 2 simulations: (1) a polluted aerosol scenario with anthropogenic aerosols accounted which is for the real situation; (2) an assumptive clean scenario without anthropogenic aerosols. Domain 2 is run with initial and lateral boundary chemical and aerosols fields from Domain 1 outputs and initial and lateral boundary meteorological conditions from MERRA-2. Note that we use the meteorology from MERRA-2 as the initial and lateral boundary conditions for Domain 2 instead of Domain 1 outputs, because we want to keep the initial and lateral boundary meteorological conditions the same for

all the sensitivity tests with different microphysics and aerosol setups (meteorology is different between the two simulations over Domain 1).

The simulations in Domain 1 were initiated at 0000 UTC on 14 Jun and ended at 1200 UTC 20 June with about 5 days for the chemistry spin-up. The meteorological field was reinitialized every 36 hours to prevent the model drifting. The dynamic time step was 6 s for Domain 1 and 3 s for Domain 2. The anthropogenic emission was from NEI-2011 emissions. The biogenic emission came from the Model of Emissions of Gases and Aerosols from Nature (MEGAN) product (Guenther et al., 2006). The biomass burning emission was from the Fire Inventory from NCAR (FINN) model (Wiedinmyer et al., 2011). We used the Carbon Bond Mechanism Z (CBMZ) gas-phase chemistry (Zaveri and Peters, 1999) and MOSAIC aerosol model with four bins (Zaveri et al., 2008). The physics schemes other than microphysics applied in the simulation are the Unified Noah land surface scheme (Chen and Dudhia, 2001), Mellor-Yamada-Janjic planetary boundary layer scheme (Janjic et al., 1994), Multi-layer, Building Environment Parameterization (BEP) urban physics scheme (Salamanca and Martilli, 2010), the RRTMG longwave and shortwave radiation schemes (Iacono et al., 2008).

The main purpose of the simulations in Domain 1 is to provide initial and boundary chemical and aerosol conditions for the simulations in Domain 2. To save computational cost, WRF-Chem coupled with Morrison two-moment bulk microphysics scheme (Morrison et al., 2005) is used for the simulations in Domain 1. Two simulations run for Domain 1 are referred to as D1_MOR_anth in which the anthropogenic emissions are turned on and D1_MOR_noanth where the anthropogenic emissions are turned off. Then four major experiments are carried out to simulate the convective event near Houston over Domain 2 with two cloud microphysics schemes and two aerosol scenarios, respectively. We refer to the simulation in which SBM is used and the

215 anthropogenic emissions are included using the initial and boundary chemicals and aerosols from
216 D1_MOR_anth, as our baseline simulation (referred to as “SBM_anth”). SBM_noanth is based on
217 SBM_anth but uses initial and boundary chemicals and aerosols from D1_MOR_noanth and turns
218 off the anthropogenic emissions, meaning that anthropogenic aerosols are not taken into account.
219 MOR_anth and MOR_noanth are the two corresponding simulations to SBM_anth and
220 SBM_noanth, respectively, using the Morrison two-moment bulk microphysics scheme. To
221 examine the contribution of the saturation adjustment approach for condensation and evaporation
222 to the simulated aerosol effects with the Morrison scheme, we further conducted two sensitivity
223 tests, based on MOR_anth and MOR_noanth, by replacing the saturation adjustment approach in
224 the Morrison scheme with the condensation and evaporation calculation based on an explicit
225 representation of supersaturation over a time step as described in Lebo et al. (2012). That is the
226 supersaturation is solved by the source and sink in terms of dynamic forcing and
227 condensation/evaporation within a one-timestep. Note in both SBM and this modified Morrison
228 schemes, the supersaturation for condensation and evaporation is calculated after the advection.
229 These two simulations are referred to as MOR_SS_anth and MOR_SS_noanth, respectively. To
230 present more robust results, we carry out a small number of ensembles (three) for each case over
231 Domain 2 (we do not have computer time to do more ensemble runs). The three ensemble runs are
232 only different in the initialization time: 0000 UTC, 0600 UTC, and 1200 UTC on 19 June. All the
233 simulations end at 1200 UTC 20 June. The analysis results for Domain 2 simulations in this study
234 are based on the mean values of three ensemble runs and the ensemble spread is shown as the
235 shaded area in all profile figures.

We evaluate the aerosol and CCN properties simulated by D1_MOR_anth to ensure realistic aerosol fields, which are used for the Domain 2 simulations with anthropogenic aerosols considered. These evaluations are included in section 4.1.

From D1_MOR_anth, we see a very large spatial variability of aerosol number concentrations (Fig. 2b). There are three regions with significantly different aerosol loadings over the domain as shown by the black boxes in Fig. 2b: (a) the Houston urban area, (b) the rural area about 100 km northeast of Houston, and (c) the Gulf of Mexico. Aerosols over the Houston urban area are mainly contributed by organic aerosols, which are highly related to industrial and ship channel emissions. The rural area aerosols are mainly from sulfate and sea salt aerosol is the major contributor over the Gulf of Mexico. This suggests that aerosol properties are extremely heterogeneous in this region. The aerosols over Houston urban area are generally about 5 and 10 times higher than the rural and Gulf area, respectively (Fig. 2c). The size distributions show a three-mode distribution with the largest differences from the Aitken mode (peaks at 50 nm; Fig. 2c). These ultrafine aerosol particles are mainly contributed by anthropogenic activities (Fig. 2b, d). With the anthropogenic emissions turned off, the simulated aerosols are much lower and have much less spatial variability (Fig. 2d).

4 Result

4.1 Model Evaluation

We first show the evaluation of the aerosol and CCN properties simulated by D1_MOR_anth, which runs over Domain 1, much larger than Domain 2. As described in Table 1, there are eight PM monitoring sites from TCEQ around the Houston area. Surface PM_{2.5} shows high concentrations at Houston and its downwind regions (Fig. 3). D1_MOR_anth shows a similar

spatial pattern with the observations in terms of the surface PM_{2.5} averaged over 24 hours (the day before the convection near Houston), although with a difficulty to reproduce the values for some sites. The hourly variations of ground-level PM_{2.5} concentrations from both observation and D1_MOR_anth for these sites in the day before the convective initiation is depicted in Fig. 4. Generally, the simulated hourly pattern agrees with the observation for eight stations. D1_MOR_anth reproduces the diurnal variations, especially the increasing trend from 1200 UTC to 1800 UTC 19 Jun prior to the initiation of deep convective cells over Houston and Galveston bay areas.

The evaluation of the cloud base heights and CCN at cloud bases at the warm cloud stage before transitioning to deep clouds (2000 UTC) are shown in Fig.5. Over Houston and its surrounding area (black box in Fig. 5), the simulated cloud base heights are about 1.5-2 km, in an agreement with the retrieved values from VIIRS satellite, which are around 1.2-1.8 km (Fig. 5a-b). The retrieved CCN concentrations at cloud bases vary significantly over the domain and this spatial variability is generally captured by the model (Fig. 5c-d). For example, D1_MOR_anth simulates some high CCN concentrations (400-800 cm⁻³ with some above 1000 cm⁻³) over the Houston and around the Bay area, relatively low CCN values in the rural areas (about 200-600 cm⁻³), and very low values over the Gulf of Mexico (less than 200 cm⁻³), as shown in Fig. 5d. This is consistent with the spatial variability from the retrievals (Fig. 5c). The evaluation of aerosol properties before the initiation of Houston convective cells and CCN at the warm cloud stage before transitioning to deep clouds provides us confidence in using the chemical and aerosol fields from Domain 1 outputs to feed Domain 2 simulations.

Now we are evaluating near-surface temperature and winds, reflectivity and precipitation simulated by SBM_anth and MOR_anth. Fig. 6 shows the comparisons in 2-m temperature and

10-m winds at 1800 UTC (before the convective initiation). Compared with the coarse resolution NLDAS data, both SBM_anth and MOR_anth capture the general temperature pattern with a little overestimation in the northeast part of the domain (mainly rural area). The modeled southerly winds do not reach further north as the NLDAS data, possibly because of the feedback of the small-scale features which are simulated with the high resolution to mesoscale circulations. However, the simulation of temperature over Houston and sea breeze winds from the Gulf of Mexico to Houston is the most important in this case. SBM_anth predicts a slightly higher temperature than MOR_anth in the northern part of the Houston region (purple box in Fig. 6), which agrees with NLDAS better. SBM_anth gets similar southerly winds from the Gulf of Mexico to Houston as shown in NLDAS, while the southerly winds from the Gulf of Mexico become very weak or disappear prior to reaching Houston in MOR_anth.

For the Houston convective cell that we focused (red box in Fig. 7a), SBM_anth simulates it well in both location and high reflectivity value (greater than 50 dBZ) in comparison with the NEXRAD observation (Fig. 7a, b, d, f). The simulated composite reflectivities (i.e., the column maximum) are up to 55-60 dBZ from all three ensemble members, consistent with NEXRAD. With the Morrison scheme, MOR_anth simulates several small convective cells near Houston with a maximum reflectivity of 55 dBZ or less (Fig. 7c, e, g). All three ensemble members consistently show smaller but more scattered convective cells with the Morrison scheme compared with SBM. The contoured frequency by altitude diagram (CFAD) plots for the entire storm period show that SBM_anth is in a better agreement with observation compared with MOR_anth, especially for the vertical structure of the high reflectivity range (greater than 48 dBZ, black dashed lines in Fig. 8) and echo top heights, which can reach up to 14-15 km (Fig. 8a-b). MOR_anth overestimates the occurrence frequencies of the 35-45 dBZ range and underestimates those of the low and high

reflectivity ranges (less than 15 dBZ or larger than 50 dBZ) as well as the echo top heights (1-2 km lower than SBM_anth; Fig. 8c).

For the precipitation rates averaged over the study area (red box in Fig. 7), the observation shows two peaks, which are captured by both SBM_anth and MOR_anth (Fig. 9a). However, the timing for the first peak is about 30 and 60 min earlier in SBM_anth and MOR_anth than the observation, respectively. Also, SBM_anth predicts the rain rate intensities at the two peak times more consistent with the observations whereas MOR_anth underestimates the rain rate intensity at the second peak time (Fig. 9a). The large precipitation rates (greater than 15 mm h^{-1}) in SBM_anth has a ~ 1.5 times larger occurrence probability than those in MOR_anth, showing a better agreement with the observation (Fig. 9b). The observed accumulated rain over the time period shown in Fig. 9a is about 3.8 mm, both SBM_anth ($\sim 4.5 \text{ mm}$) and MOR_anth ($\sim 4.2 \text{ mm}$) overestimate the accumulated precipitation due to the longer rain period compared with the observations. Overall, the performance of SBM_anth is superior to MOR_anth in simulating the location and intensity of the convective storm and associated precipitation by comparing with the observation.

4.2 Simulated Aerosol Effects on Cloud and Precipitation

Now we look at the effects of anthropogenic aerosols on the deep convective storm simulated with SBM and Morrison microphysics schemes. Fig. 9a shows that with the SBM scheme, anthropogenic aerosols remarkably increase the mean surface rain rates (by $\sim 30\%$; from SBM_noanth to SBM_anth), mainly because of the increased occurrence frequency (nearly doubled) for relatively large rain rates (i.e., $10\text{--}15 \text{ mm h}^{-1}$ and $>15 \text{ mm h}^{-1}$) in Fig. 9b. With the Morrison scheme, the changes in mean precipitation and the PDF from MOR_noanth to MOR_anth are relatively small, showing a very limited aerosol effect on precipitation. Both SBM

and Morrison schemes show higher occurrences of large precipitation rates ($> 10 \text{ mm h}^{-1}$) and lower occurrences of small precipitation rates ($< 10 \text{ mm h}^{-1}$) due to anthropogenic aerosols (Fig. 9b), but the effect is larger with SBM. For the accumulated precipitation, the anthropogenic aerosols lead to a $\sim 0.5 \text{ mm}$ increase over the storm period with the SBM scheme, while only a $\sim 0.2 \text{ mm}$ increase with the Morrison scheme. Note Fig. 9a shows that anthropogenic aerosols lead to an earlier start of the precipitation with both SBM and Morrison, which reflects the faster transition of warm rain to mixed-phase precipitation. We do see the delay of warm rain by aerosols but only about 5 min (probably due to the humid condition of the case), which is difficult to be shown in Fig. 9a since the averaged rain rate for the analysis box is $\sim 0.02 \text{ mm hr}^{-1}$ and the time period is very short ($\sim 10 \text{ min}$).

With the SBM scheme, the increase in the updraft speeds by the anthropogenic aerosols is even more notable than the precipitation (Fig. 10a-b). Above 5-km altitude, the occurrence frequencies of updraft speed greater than 0.4% extend to much larger values, with 36 m s^{-1} at the upper levels in SBM_anth while only $\sim 20 \text{ m s}^{-1}$ in SBM_noanth. With the Morrison scheme, the changes are not significant by the anthropogenic aerosols (MOR_noanth vs MOR_anth in Fig. 10c-d). From MOR_noanth to MOR_anth, there is a slight increase in updraft speed at around 9-11 km altitudes but a slight decrease at 6-8 km altitudes. The significant invigoration of convective intensity by anthropogenic aerosols with the SBM scheme explains the much larger occurrences of relatively large rain rates and overall more surface precipitation due to the anthropogenic aerosol effect (Fig. 9).

Now the question is why the anthropogenic aerosols enhance the convective intensity of the storm with the SBM scheme while the effect is very small with the Morrison scheme. Fig. 11 shows the vertical profiles of mean updraft velocity, buoyancy, and total latent heating rate of the

350 top 25th percentile updrafts with a value greater than 2 m s^{-1} during the deep convective cloud
 351 stage. Both SBM and MORR show similar vertical structures of convective intensity but the
 352 convective intensity with the Morrison scheme is weaker than SBM in the case with anthropogenic
 353 aerosols considered, especially at high altitudes. With the SBM microphysics scheme, the
 354 increased convective intensity due to the anthropogenic aerosol effect corresponds to the increased
 355 buoyancy ($\sim 30\%$) from SBM_noanth to SBM_anth (Fig. 11a, c). The increased buoyancy can be
 356 explained by the increased total latent heating (Fig. 11e). From SBM_noanth to SBM_anth, the
 357 increase in latent heating from both condensation and ice-related microphysical processes
 358 (including deposition, drop freezing, and riming) are significant, with the increase from
 359 condensation latent heating is relatively larger (about 60% more as shown in Fig. 12a). As shown
 360 in Fan et al., (2018), the increase in lower-level condensation latent heating has a much larger
 361 effect on intensifying updraft intensity compared with the same amount of increase in high-level
 362 latent heating from ice-related microphysical processes. Thus, the convective invigoration by the
 363 anthropogenic aerosols with the SBM scheme is through both warm-phase invigoration and cold-
 364 phase invigoration, with the former playing a more important role. Compared with the Morrison
 365 scheme, the increase of total latent heating by the anthropogenic aerosols is almost doubled with
 366 the SBM scheme, explaining more remarkable enhancement of buoyancy and thus the convective
 367 intensity (red lines vs blue lines in Fig. 11). From MOR_noanth to MOR_anth, there is a small
 368 increase in both the condensation latent heating and high-level latent heating associated with ice-
 369 related processes (blue lines in Fig. 12b). As shown in Fig. 12, the difference in the increase of
 370 latent heating by the anthropogenic aerosols between SBM and Morrison schemes comes from
 371 both condensation latent heating (with a $\sim 20\%$ increase with SBM but only $\sim 8\%$ with Morrison)
 372 and ice-related processes latent heating (with a $\sim 13\%$ increase with SBM and $\sim 10\%$ with

Morrison), with the major differences from condensation latent heating. The small increase in condensation latent heating limits convective invigoration by aerosols with the Morrison scheme.

To understand why the responses of condensation to the anthropogenic aerosols are different between the SBM and Morrison schemes, we look into the process rates of drop nucleation and condensation (Fig. 13). The calculations of aerosol activation and condensation/evaporation in the SBM scheme are based on the Köhler theory and diffusional growth equations in light of particle size and supersaturation, receptively. Whereas in the Morrison scheme, the Abdul-Razzak and Ghan (2002) parameterization is used for aerosol activation and the saturation adjustment method is applied for condensation and evaporation calculation. With the SBM scheme, the anthropogenic aerosols increase the drop nucleation rates by a few times over the profile (red lines in Fig. 13a), and the condensation rates (i.e., the rate of gain in cloud water due to water vapor condensation) are also drastically increased (doubled between 4-6 km altitudes as shown in Fig. 13c). The enhanced condensation rate by the anthropogenic aerosols is because much more aerosols are activated to form a larger number of small droplets, increasing the integrated droplet surface area for condensation, as documented in Fan et al., (2018). As a result, supersaturation is drastically lower in SBM_anth than SBM_noanth (green lines in Fig. 13a). With the Morrison scheme, similarly to SBM, a large increase in the droplet nucleation rate is seen (Fig. 13b). However, the condensation rates are barely increased (blue solid vs. dashed lines in Fig. 13d). We hypothesize that the lack of response of condensation to the increased aerosol activation with the Morrison scheme is mainly because of the saturation adjustment calculation of the condensation and evaporation process. The approach does not allow supersaturation in the cloud and the calculation of condensation does not depend on supersaturation and droplet properties, thus removes the sensitivity to the anthropogenic aerosols.

To verify our hypothesis and examine how much the saturation adjustment method is responsible for the weak responses of condensation latent heating and convection to the added anthropogenic aerosols, we conducted two additional sensitivity tests by replacing the saturation adjustment approach in the Morrison scheme with the condensation and evaporation calculation based on an explicit representation of supersaturation over a time step, as described in Section 3. The result shows that the modified Morrison scheme with the explicit supersaturation leads to (1) larger condensation rates and latent heating (Figs. 12b and 13d) and (2) a larger anthropogenic aerosol effect on condensation and ice-related processes, compared with the saturation adjustment approach.

First, we explain why the explicit supersaturation leads to larger condensation rates and latent heating than the saturation adjustment. The time evolution of latent heating, updraft, and hydrometeor properties is examined (Fig. S1). At the warm cloud stage at 1700 UTC, the saturation adjustment produces more condensation latent heating which leads to larger buoyancy and stronger updraft intensity compared to the explicit supersaturation because of removing supersaturation (Fig. S1, left, blue vs. orange). However, by the time of 1900 UTC when the clouds have developed into mixed-phase clouds, the saturation adjustment produces smaller condensational heating and weaker convection than the explicit supersaturation approach (Fig. S1, middle). The results remain similarly later at the deep cloud stage 2100 UTC (Fig. S1, right). How does this change happen from 1700 to 1900 UTC? At the warm cloud stage (1700 UTC), the saturation adjustment produces droplets with larger sizes (up to 100% larger for the mean radius) than the explicit supersaturation because of more cloud water produced as a result of zeroing-out supersaturation at each time step (droplet formation is similar between the two cases as shown in Fig. 13). This results in the much faster and larger warm rain, while with the explicit supersaturation rain number and mass are

absent at 1700 UTC as shown in Fig. S2d and S3d). As a result, when evolving into the mixed-phase stage (1900 UTC), much fewer cloud droplets are transported to the levels above the freezing level (Fig. S2b and S3b). Whereas with the explicit supersaturation, because of the delayed/suppressed warm rain and smaller droplets (the mean radius is decreased from 8 to 6 μm at 3 km), much more cloud droplets are lifted to the higher levels. Correspondingly, a few times higher total ice particle number and mass are seen compared with the saturation adjustment (Fig. S2g and S3g) because more droplets above the freezing level induce stronger ice processes (droplet freezing, riming, and deposition). This leads to more latent heat release (Fig. S1e), which increases the buoyancy and convective intensity. When convection is stronger, more condensation occurs thus a larger condensation latent heating is seen with the explicit supersaturation.

Now we explain why the explicit supersaturation leads to a larger aerosol effect on convective intensity compared with the saturation adjustment approach. First, the enhancement of condensational heating is larger by aerosols with the explicit supersaturation (Fig. S1a-c), mainly because the condensation depends on supersaturation and droplet properties, while the saturation adjustment approach removes the dependence of condensation on droplet properties. Second, increasing aerosols with the explicit supersaturation leads to a larger enhancement of ice-related processes (Fig. S1b-c) due to a larger reduction in droplet size (up to 1 μm more in the mean radius) than the saturation adjustment. The enhanced convective intensity would further lead to a larger enhancement in condensational heating. Therefore, we see a much larger aerosol effect with the explicit supersaturation than with the saturation adjustment because of more enhanced condensation latent heating and ice-related latent heating. The increase in condensation latent heating and ice-related latent heating by the anthropogenic aerosols with explicit supersaturation is comparable to SBM (orange lines vs red lines in Figure 12), resulting in a similarly large increase

in buoyancy and thus convective intensity (orange lines vs red lines in Fig. 11). The increase of precipitation by aerosols is also similar to that with the SBM scheme (not shown).

With enhanced convection by anthropogenic aerosols, the responses of hydrometeor mass and number are significant. With the SBM scheme, the increases in mass and number of cloud droplets, raindrops, and total ice particles (ice, snow, and graupel) by the anthropogenic aerosols are very significant (Fig. 14-15, left, red lines). The increases in the total ice mass and number are particularly significant ($\sim 35\%$ in mass and $\sim 30\%$ in number). The mass increase in frozen hydrometeors is mainly contributed by graupel (Fig. S4, left, red lines) while the number increase mainly comes from cloud ice (Fig. S5, red lines). This suggests a large effect of enhanced convective intensity on frozen hydrometeors and thus precipitation. With the Morrison scheme, little change is seen (Fig. 14-15 and Fig. S4-S5, right, blue lines). By replacing the saturation adjustment with the explicit supersaturation for condensation and evaporation, the increases in those hydrometeor masses and numbers become consistent with the SBM scheme (Fig. 14-15 and Fig. S4-S5, orange lines and red lines).

These results verify that the saturation adjustment approach for parameterizing condensation and evaporation is the major reason responsible for limited aerosol effects on convective intensity and precipitation with the original Morrison scheme. Past studies also showed the limitations of the saturation adjustment approach in simulating aerosol impacts on deep convective clouds (e.g., Fan et al., 2016; Lebo et al., 2012; Lee et al., 2018; Wang et al., 2013).

5 Conclusions and Discussion

We have conducted model simulations of a deep convective cloud case occurring on 19 June 2013 over the Houston area with WRF-Chem coupled with the SBM and Morrison microphysics schemes to (1) evaluate the performance of WRF-Chem-SBM in simulating the deep convective

clouds, and (2) explore the differences in aerosol effects on the deep convective clouds produced by the SBM and Morrison schemes and the major factors responsible for the differences.

We have evaluated the simulated aerosols, CCN, cloud base heights, reflectivity, and precipitation. The model simulates the large spatial variability of aerosols and CCN from the Gulf of Mexico, rural areas, to Houston city. On the bulk magnitudes, the model captures the surface PM_{2.5}, cloud base height, and CCN at cloud bases near Houston reasonably well. These realistically simulated aerosol fields were fed to higher resolution simulations (0.5 km) using the SBM and Morrison schemes. With the SBM scheme, the model simulates a deep convective cloud over Houston in a better agreement with the observed radar reflectivity and precipitation, compared with using the Morrison scheme. Indeed, both schemes show similar vertical structures of convective intensity and hydrometeor properties, with a weaker updraft intensity with the Morrison scheme at high altitudes in the case with anthropogenic aerosols considered.

Replacing the saturation adjustment for the condensation and evaporation calculation with an explicit supersaturation approach leads to an increase in updraft intensity, resulting in similar results as SBM for the case with anthropogenic aerosols considered. This is because with the explicit supersaturation approach droplet sizes are smaller in the warm cloud stage than the saturation adjustment which condenses all supersaturation. The less efficient conversion of cloud droplets to rain allows more cloud droplets to be transported to the altitudes above the freezing level at the mixed-phase and deep cloud stages, inducing stronger ice microphysical processes (freezing, riming, and deposition) and invigorating convection. Lebo et al. (2012) showed a similar feature that the saturation adjustment has larger total condensate mass at the beginning but less at the later stage compared to the explicit supersaturation approach, particularly in total ice mass. In addition, Grabowski and Morrison (2017) showed that the saturation adjustment affected ice

processes in another way by producing larger ice particles with larger falling velocities compared with the explicit supersaturation approach, leading to the reduction of anvil clouds.

About the anthropogenic aerosol effects, with the SBM scheme, anthropogenic aerosols notably increase the convective intensity, enhance the peak precipitation rate over the Houston area (by $\sim 30\%$), and double the frequencies of relatively large rain rates ($> 10 \text{ mm h}^{-1}$). The enhanced convective intensity by anthropogenic aerosols makes the simulated storm agree better with the observed, mainly attributed to the increased condensation and ice-related latent heating, with the former is more significant. In contrast, with the Morrison scheme, there is no significant anthropogenic aerosol effect on the convective intensity and total precipitation. But the Morrison schemes indeed shows a qualitatively consistent results with SBM in aerosol effects on the PDF of rain rates: higher occurrences of large precipitation rates ($> 10 \text{ mm h}^{-1}$) and lower occurrences of small precipitation rates ($< 10 \text{ mm h}^{-1}$).

By replacing the saturation adjustment with an explicit supersaturation approach for the condensation and evaporation calculation, the modified Morrison shows much larger anthropogenic aerosol effects on convective intensity, hydrometeor properties, and precipitation than the original Morrison scheme, and those aerosol effects are similar to the SBM scheme. Therefore, the saturation adjustment method for the condensation and evaporation calculation is mainly responsible for the limited aerosol effects with the Morrison scheme. This is mainly because the saturation adjustment approach limits the enhancement in (1) condensation latent heat by removing the dependence of condensation on droplet properties and (2) the ice-related processes by a more efficient conversion of droplets into raindrops, which leads to fewer cloud droplets being transported to the altitudes above the freezing level. Therefore, the explicit supersaturation enhances aerosol effects through enhanced condensation and cold-phase processes,

but enhanced condensation should play a more important role. This study suggests, when the computational resource is not sufficient or in other situations such as the application of SBM is not available, the Morrison scheme modified with the condensation and evaporation calculation based on a simple representation of supersaturation can be applied to study aerosol effects on convective clouds, especially for warm and humid cloud cases in which the response of condensation to aerosols is particularly important.

Following Fan et al., (2018), which showed that the warm-phase invigoration mechanism was manifested by ultrafine aerosol particles in the Amazon warm and humid environment with extremely low background aerosol particles. Here we showed that in summer anthropogenic aerosols over the Houston area may also enhance the thunderstorm intensity and precipitation through the same mechanism by secondary nucleation of numerous ultrafine aerosol particles from the anthropogenic sources. But the magnitude of the effect is not as substantial as in the Amazon environment. Possible reasons include that background aerosols are much higher over the Houston area and air is not as humid as Amazon.

Acknowledgments

This study is supported by the U.S. Department of Energy Office of Science through its Early Career Award Program and a grant DE-SC0018996 and the NSF (AGS1837811). PNNL is operated for the US Department of Energy (DOE) by Battelle Memorial Institute under Contract DE-AC05-76RL01830. This research used resources of PNNL Institutional Computing (PIC), and the National Energy Research Scientific Computing Center (NERSC), a U.S. Department of Energy Office of Science User Facility operated under contract DE-AC02-05CH11231. We thank Chun Zhao at China University of Science and Technology for providing the quasi-global WRF-

533 Chem simulation data, and Hugh Morrison at the National Center for Atmospheric Research for
534 the Morrison code with supersaturation-forced condensation and evaporation calculation.
535

Reference

- Abdul-Razzak, H., and Ghan, S. J.: A parameterization of aerosol activation - 3. Sectional representation, *J Geophys Res-Atmos*, 107, 4026, doi: 10.1029/2001jd000483, 2002.
- Andreae, M. O., Jones, C. D., and Cox, P. M.: Strong present-day aerosol cooling implies a hot future, *Nature*, 435, 1187-1190, doi: 10.1038/nature03671, 2005.
- Arakawa, A.: The cumulus parameterization problem: Past, present, and future, *J Climate*, 17, 2493-2525, doi: 10.1175/1520-0442(2004)017<2493:Ratcpp>2.0.Co;2, 2004.
- Chen, F., and Dudhia, J.: Coupling an advanced land surface-hydrology model with the Penn State-NCAR MM5 modeling system. Part I: Model implementation and sensitivity, *Mon Weather Rev*, 129, 569-585, doi: 10.1175/1520-0493(2001)129<0569:Caalsh>2.0.Co;2, 2001.
- Chen Q., J. Fan, Y. Yin, and B. Han: Aerosol impacts on mesoscale convective systems forming under different vertical wind shear conditions. *Journal of Geophysical Research: Atmospheres*, 125, e2018JD030027, 2020.
- Chen, Y. C., Xue, L., Lebo, Z. J., Wang, H., Rasmussen, R. M., and Seinfeld, J. H.: A comprehensive numerical study of aerosol-cloud-precipitation interactions in marine stratocumulus, *Atmos Chem Phys*, 11, 9749-9769, doi: 10.5194/acp-11-9749-2011, 2011.
- Dagan, G., Koren, I., Altaratz, O. and Lehahn, Y.: Shallow convective cloud field lifetime as a key factor for evaluating aerosol effects. *iScience*, 10, 192–202, 2018.
- Ekman, A. M. L., Engstrom, A., and Soderberg, A.: Impact of Two-Way Aerosol-Cloud Interaction and Changes in Aerosol Size Distribution on Simulated Aerosol-Induced Deep Convective Cloud Sensitivity, *J Atmos Sci*, 68, 685-698, doi: 10.1175/2010jas3651.1, 2011.

559 Fan, J. W., Zhang, R. Y., Li, G. H., and Tao, W. K.: Effects of aerosols and relative humidity on
 560 cumulus clouds, *J Geophys Res-Atmos*, 112, D14204, doi: 10.1029/2006jd008136, 2007.

561 Fan, J. W., Yuan, T. L., Comstock, J. M., Ghan, S., Khain, A., Leung, L. R., Li, Z. Q., Martins, V.
 562 J., and Ovchinnikov, M.: Dominant role by vertical wind shear in regulating aerosol effects
 563 on deep convective clouds, *J Geophys Res-Atmos*, 114, D22206, doi:
 564 10.1029/2009jd012352, 2009.

565 Fan, J. W., Leung, L. R., Li, Z. Q., Morrison, H., Chen, H. B., Zhou, Y. Q., Qian, Y., and Wang,
 566 Y.: Aerosol impacts on clouds and precipitation in eastern China: Results from bin and
 567 bulk microphysics, *J Geophys Res-Atmos*, 117, D00k36, doi: 10.1029/2011jd016537,
 568 2012a.

569 Fan, J. W., Rosenfeld, D., Ding, Y. N., Leung, L. R., and Li, Z. Q.: Potential aerosol indirect effects
 570 on atmospheric circulation and radiative forcing through deep convection, *Geophys Res*
 571 *Lett*, 39, L09806, doi: 10.1029/2012gl051851, 2012b.

572 Fan, J. W., Leung, L. R., Rosenfeld, D., Chen, Q., Li, Z. Q., Zhang, J. Q., and Yan, H. R.:
 573 Microphysical effects determine macrophysical response for aerosol impacts on deep
 574 convective clouds, *P Natl Acad Sci USA*, 110, E4581-E4590, doi:
 575 10.1073/pnas.1316830110, 2013.

576 Fan, J. W., Wang, Y., Rosenfeld, D., and Liu, X. H.: Review of Aerosol-Cloud Interactions:
 577 Mechanisms, Significance, and Challenges, *J Atmos Sci*, 73, 4221-4252, doi: 10.1175/Jas-
 578 D-16-0037.1, 2016.

579 Fan, J. W., Han, B., Varble, A., Morrison, H., North, K., Kollias, P., Chen, B. J., Dong, X. Q.,
 580 Giangrande, S. E., Khain, A., Lin, Y., Mansell, E., Milbrandt, J. A., Stenz, R., Thompson,
 581 G., and Wang, Y.: Cloud-resolving model intercomparison of an MC3E squall line case:

582 Part I-Convective updrafts, *J Geophys Res-Atmos*, 122, 9351-9378, doi:
583 10.1002/2017jd026622, 2017.

584 Fan, J. W., Rosenfeld, D., Zhang, Y. W., Giangrande, S. E., Li, Z. Q., Machado, L. A. T., Martin,
585 S. T., Yang, Y., Wang, J., Artaxo, P., Barbosa, H. M. J., Braga, R. C., Comstock, J. M.,
586 Feng, Z., Gao, W. H., Gomes, H. B., Mei, F., Pohlker, C., Pohlker, M. L., Poschl, U., and
587 de Souza, R. A. F.: Substantial convection and precipitation enhancements by ultrafine
588 aerosol particles, *Science*, 359, 411-418, doi: 10.1126/science.aan8461, 2018.

589 Fast, J. D., Gustafson, W. I., Easter, R. C., Zaveri, R. A., Barnard, J. C., Chapman, E. G., Grell, G.
590 A., and Peckham, S. E.: Evolution of ozone, particulates, and aerosol direct radiative
591 forcing in the vicinity of Houston using a fully coupled meteorology-chemistry-aerosol
592 model, *J Geophys Res-Atmos*, 111, D21305, doi: 10.1029/2005jd006721, 2006.

593 Gao, W. H., Fan, J. W., Easter, R. C., Yang, Q., Zhao, C., and Ghan, S. J.: Coupling spectral-bin
594 cloud microphysics with the MOSAIC aerosol model in WRF-Chem: Methodology and
595 results for marine stratocumulus clouds, *J Adv Model Earth Sy*, 8, 1289-1309, doi:
596 10.1002/2016ms000676, 2016.

597 Gelaro, R., McCarty, W., Suarez, M. J., Todling, R., Molod, A., Takacs, L., Randles, C. A.,
598 Darmenov, A., Bosilovich, M. G., Reichle, R., Wargan, K., Coy, L., Cullather, R., Draper,
599 C., Akella, S., Buchard, V., Conaty, A., da Silva, A. M., Gu, W., Kim, G. K., Koster, R.,
600 Lucchesi, R., Merkova, D., Nielsen, J. E., Partyka, G., Pawson, S., Putman, W., Rienecker,
601 M., Schubert, S. D., Sienkiewicz, M., and Zhao, B.: The Modern-Era Retrospective
602 Analysis for Research and Applications, Version 2 (MERRA-2), *J Climate*, 30, 5419-5454,
603 doi: 10.1175/Jcli-D-16-0758.1, 2017.

604 Grabowski, W. W., and H. Morrison: Untangling microphysical impacts on deep convection
 605 applying a novel modeling methodology. Part II: Double-moment microphysics. *J. Atmos.*
 606 *Sci.*, 73, 3749–3770, 2016.

607 Grabowski, W. W., and H. Morrison: Modeling condensation in deep convection, *J. Atmos.*
 608 *Sci.*, 74, 2247– 2267, doi:10.1175/JAS-D-16-0255.1, 2017.

609 Grabowski, W. W., and H. Morrison: Do ultrafine cloud condensation nuclei invigorate deep
 610 convection? *J. Atmos. Sci.*, 77(7), 2567-2583, doi: 10.1175/JAS-D-20-0012.1, 2020.

611 Grell, G. A., Peckham, S. E., Schmitz, R., McKeen, S. A., Frost, G., Skamarock, W. C., and Eder,
 612 B.: Fully coupled "online" chemistry within the WRF model, *Atmos Environ*, 39, 6957-
 613 6975, doi: 10.1016/j.atmosenv.2005.04.027, 2005.

614 Guenther, A., Karl, T., Harley, P., Wiedinmyer, C., Palmer, P. I., and Geron, C.: Estimates of
 615 global terrestrial isoprene emissions using MEGAN (Model of Emissions of Gases and
 616 Aerosols from Nature), *Atmos Chem Phys*, 6, 3181-3210, doi: 10.5194/acp-6-3181-2006,
 617 2006.

618 Haywood, J., and Boucher, O.: Estimates of the direct and indirect radiative forcing due to
 619 tropospheric aerosols: A review, *Rev Geophys*, 38, 513-543, doi: 10.1029/1999rg000078,
 620 2000.

621 Houze, R. A.: *Cloud dynamics*, 2. edn., Elsevier/Acad. Press, Amsterdam, 2014.

622 Iacono, M. J., Delamere, J. S., Mlawer, E. J., Shephard, M. W., Clough, S. A., and Collins, W. D.:
 623 Radiative forcing by long-lived greenhouse gases: Calculations with the AER radiative
 624 transfer models, *J Geophys Res-Atmos*, 113, D13103, doi: 10.1029/2008jd009944, 2008.

625 Janjic, Z. I.: The Step-Mountain Eta Coordinate Model - Further Developments of the Convection,
 626 Viscous Sublayer, and Turbulence Closure Schemes, Mon Weather Rev, 122, 927-945, doi:
 627 10.1175/1520-0493(1994)122<0927:Tsmecm>2.0.Co;2, 1994.

628 Khain, A., Pokrovsky, A., Pinsky, M., Seifert, A., and Phillips, V.: Simulation of effects of
 629 atmospheric aerosols on deep turbulent convective clouds using a spectral microphysics
 630 mixed-phase cumulus cloud model. Part I: Model description and possible applications, J
 631 Atmos Sci, 61, 2963-2982, doi: 10.1175/Jas-3350.1, 2004.

632 Khain, A., Rosenfeld, D., and Pokrovsky, A.: Aerosol impact on the dynamics and microphysics
 633 of deep convective clouds, Q J Roy Meteor Soc, 131, 2639-2663, doi: 10.1256/qj.04.62,
 634 2005.

635 Khain, A., and Lynn, B.: Simulation of a supercell storm in clean and dirty atmosphere using
 636 weather research and forecast model with spectral bin microphysics, J Geophys Res-Atmos,
 637 114, D19209, doi: 10.1029/2009jd011827, 2009.

638 Khain, A., Lynn, B., and Dudhia, J.: Aerosol Effects on Intensity of Landfalling Hurricanes as
 639 Seen from Simulations with the WRF Model with Spectral Bin Microphysics, J Atmos Sci,
 640 67, 365-384, doi: 10.1175/2009jas3210.1, 2010.

641 Khain, A. P., BenMoshe, N., and Pokrovsky, A.: Factors determining the impact of aerosols on
 642 surface precipitation from clouds: An attempt at classification, J Atmos Sci, 65, 1721-1748,
 643 doi: 10.1175/2007jas2515.1, 2008.

644 Khain, A. P., Leung, L. R., Lynn, B., and Ghan, S.: Effects of aerosols on the dynamics and
 645 microphysics of squall lines simulated by spectral bin and bulk parameterization schemes,
 646 J Geophys Res-Atmos, 114, D22203, doi: 10.1029/2009jd011902, 2009.

647 Khain, A. P., Beheng, K. D., Heymsfield, A., Korolev, A., Krichak, S. O., Levin, Z., Pinsky, M.,
 648 Phillips, V., Prabhakaran, T., Teller, A., van den Heever, S. C., and Yano, J. I.:
 649 Representation of microphysical processes in cloud-resolving models: Spectral (bin)
 650 microphysics versus bulk parameterization, *Rev Geophys*, 53, 247-322, doi:
 651 10.1002/2014rg000468, 2015.

652 Koren, I., Dagan, G., and Altaratz, O.: From aerosol-limited to invigoration of warm convective
 653 clouds, *Science*, 344, 1143-1146, doi: 10.1126/science.1252595, 2014.

654 Korolev A., and I. Mazin: Supersaturation of water vapor in clouds. *J. Atmos. Sci.*, 60, 2957-2974,
 655 2003.

656 Lebo, Z.: A Numerical Investigation of the Potential Effects of Aerosol-Induced Warming and
 657 Updraft Width and Slope on Updraft Intensity in Deep Convective Clouds, *J Atmos Sci*,
 658 75, 535-554, doi: 10.1175/Jas-D-16-0368.1, 2018.

659 Lebo, Z. J., and Seinfeld, J. H.: Theoretical basis for convective invigoration due to increased
 660 aerosol concentration, *Atmos Chem Phys*, 11, 5407-5429, doi: 10.5194/acp-11-5407-2011,
 661 2011.

662 Lebo, Z. J., Morrison, H., and Seinfeld, J. H.: Are simulated aerosol-induced effects on deep
 663 convective clouds strongly dependent on saturation adjustment? *Atmos Chem Phys*, 12,
 664 9941-9964, doi: 10.5194/acp-12-9941-2012, 2012.

665 Lee, S. S., Li, Z. Q., Zhang, Y. W., Yoo, H., Kim, S., Kim, B. G., Choi, Y. S., Mok, J., Um, J.,
 666 Choi, K. O., and Dong, D. H.: Effects of model resolution and parameterizations on the
 667 simulations of clouds, precipitation, and their interactions with aerosols, *Atmos Chem Phys*,
 668 18, 13-29, doi: 10.5194/acp-18-13-2018, 2018.

669 Li, G. H., Wang, Y., and Zhang, R. Y.: Implementation of a two-moment bulk microphysics
 670 scheme to the WRF model to investigate aerosol-cloud interaction, *J Geophys Res-Atmos*,
 671 113, D15211, doi: 10.1029/2007jd009361, 2008.

672 Li, X. W., Tao, W. K., Khain, A. P., Simpson, J., and Johnson, D. E.: Sensitivity of a Cloud-
 673 Resolving Model to Bulk and Explicit Bin Microphysical Schemes. Part I: Comparisons, *J*
 674 *Atmos Sci*, 66, 3-21, doi: 10.1175/2008jas2646.1, 2009.

675 Li, Z. Q., Niu, F., Fan, J. W., Liu, Y. G., Rosenfeld, D., and Ding, Y. N.: Long-term impacts of
 676 aerosols on the vertical development of clouds and precipitation, *Nat Geosci*, 4, 888-894,
 677 doi: 10.1038/Ngeo1313, 2011.

678 Loftus, A. M., and Cotton, W. R.: Examination of CCN impacts on hail in a simulated supercell
 679 storm with triple-moment hail bulk microphysics, *Atmos Res*, 147, 183-204, doi:
 680 10.1016/j.atmosres.2014.04.017, 2014.

681 Lohmann, U., and Feichter, J.: Global indirect aerosol effects: a review, *Atmos Chem Phys*, 5,
 682 715-737, doi: 10.5194/acp-5-715-2005, 2005.

683 Milbrandt, J. A., and Yau, M. K.: A multimoment bulk microphysics parameterization. Part II: A
 684 proposed three-moment closure and scheme description, *J Atmos Sci*, 62, 3065-3081, doi:
 685 10.1175/Jas3535.1, 2005.

686 Morrison, H., Curry, J. A., and Khvorostyanov, V. I.: A new double-moment microphysics
 687 parameterization for application in cloud and climate models. Part I: Description, *J Atmos*
 688 *Sci*, 62, 1665-1677, doi: 10.1175/Jas3446.1, 2005.

689 Morrison, H., and W. W. Grabowski: Comparison of bulk and bin warm-rain microphysics models
 690 using a kinematic framework. *J. Atmos. Sci.*, 64, 2839–2861, 2007.

691 Morrison, H., and W. W. Grabowski: Modeling supersaturation and subgrid-scale mixing with
692 two-moment bulk warm microphysics, *J. Atmos. Sci.*, 65, 792–812,
693 doi:10.1175/2007JAS2374.1, 2008.

694 Morrison, H., Thompson, G., and Tatarskii, V.: Impact of Cloud Microphysics on the Development
695 of Trailing Stratiform Precipitation in a Simulated Squall Line: Comparison of One- and
696 Two-Moment Schemes, *Mon Weather Rev*, 137, 991-1007, doi: 10.1175/2008mwr2556.1,
697 2009.

698 Morrison, H., and Milbrandt, J.: Comparison of Two-Moment Bulk Microphysics Schemes in
699 Idealized Supercell Thunderstorm Simulations, *Mon Weather Rev*, 139, 1103-1130, doi:
700 10.1175/2010mwr3433.1, 2011.

701 Morrison, H.: On the robustness of aerosol effects on an idealized supercell storm simulated with
702 a cloud system-resolving model, *Atmos Chem Phys*, 12, 7689-7705, doi: 10.5194/acp-12-
703 7689-2012, 2012.

704 Pinsky M., I.P. Mazin, A. Korolev, and A.P. Khain: Supersaturation and diffusional droplet growth
705 in liquid clouds. *J. Atmos. Sci.* 70, 2778-2793, 2013.

706 Politovich, M. K., and W. A. Cooper: Variability of the supersaturation in cumulus clouds. *J.*
707 *Atmos. Sci.*, 45, 1651–1664, doi:10.1175/1520-0469(1988)045,1651:VOTSIC.2.0.CO;2,
708 1988.

709 Rosenfeld, D., Lohmann, U., Raga, G. B., O'Dowd, C. D., Kulmala, M., Fuzzi, S., Reissell, A.,
710 and Andreae, M. O.: Flood or drought: How do aerosols affect precipitation?, *Science*, 321,
711 1309-1313, doi: 10.1126/science.1160606, 2008.

712 Rosenfeld, D., Andreae, M. O., Asmi, A., Chin, M., de Leeuw, G., Donovan, D. P., Kahn, R.,
713 Kinne, S., Kivekas, N., Kulmala, M., Lau, W., Schmidt, K. S., Suni, T., Wagner, T., Wild,

714 M., and Quaas, J.: Global observations of aerosol-cloud-precipitation-climate interactions,
715 Rev Geophys, 52, 750-808, doi: 10.1002/2013rg000441, 2014.

716 Rosenfeld, D., Zheng, Y. T., Hashimshoni, E., Pohlker, M. L., Jefferson, A., Pohlker, C., Yu, X.,
717 Zhu, Y. N., Liu, G. H., Yue, Z. G., Fischman, B., Li, Z. Q., Giguzin, D., Goren, T., Artaxo,
718 P., Barbosa, H. M. J., Poschl, U., and Andreae, M. O.: Satellite retrieval of cloud
719 condensation nuclei concentrations by using clouds as CCN chambers, P Natl Acad Sci
720 USA, 113, 5828-5834, doi: 10.1073/pnas.1514044113, 2016.

721 Salamanca, F., and Martilli, A.: A new Building Energy Model coupled with an Urban Canopy
722 Parameterization for urban climate simulations-part II. Validation with one dimension off-
723 line simulations, Theor Appl Climatol, 99, 345-356, doi: 10.1007/s00704-009-0143-8,
724 2010.

725 Sheffield, A. M., Saleeby, S. M., and van den Heever, S. C.: Aerosol-induced mechanisms for
726 cumulus congestus growth, J Geophys Res-Atmos, 120, 8941-8952, doi:
727 10.1002/2015jd023743, 2015.

728 Skamarock, W. C., Klemp, J. B., Dudhia, J., Gill, D. O., Barker, D. M., Duda, M., Huang, X. Y.,
729 Wang, W., and Powers, J. G.: A description of the advanced research WRF version 3,
730 NCAR, Tech. Note, Mesoscale and Microscale Meteorology Division, National Center for
731 Atmospheric Research, Boulder, Colorado, USA, 2008.

732 Stevens, B., and G. Feingold: Untangling aerosol effects on clouds and precipitation in a buffered
733 system. Nature, 461, 607–613, 2009.

734 Storer, R. L., van den Heever, S. C., and Stephens, G. L.: Modeling Aerosol Impacts on Convective
735 Storms in Different Environments, J Atmos Sci, 67, 3904-3915, doi:
736 10.1175/2010jas3363.1, 2010.

- Tao, W., and X. Li: The relationship between latent heating, vertical velocity, and precipitation processes: The impact of aerosols on precipitation in organized deep convective systems, *J. Geophys. Res. Atmos.*, 121(11), 6299-6320, 2016.
- Varble A.: Erroneous attribution of deep convective invigoration to aerosol concentration. *J Atmos Sci*, 75(4):1351–68, 2018.
- van den Heever, S. C., G. L. Stephens, and N. B. Wood: Aerosol indirect effects on tropical convection characteristics under conditions of radiative-convective equilibrium. *J. Atmos. Sci.*, 68, 699–718, 2011.
- Wang, Y., Fan, J. W., Zhang, R. Y., Leung, L. R., and Franklin, C.: Improving bulk microphysics parameterizations in simulations of aerosol effects, *J Geophys Res-Atmos*, 118, 5361-5379, doi: 10.1002/jgrd.50432, 2013.
- Wiedinmyer, C., Akagi, S. K., Yokelson, R. J., Emmons, L. K., Al-Saadi, J. A., Orlando, J. J., and Soja, A. J.: The Fire INventory from NCAR (FINN): a high resolution global model to estimate the emissions from open burning, *Geosci Model Dev*, 4, 625-641, doi: 10.5194/gmd-4-625-2011, 2011.
- Yuan, T. L., Li, Z. Q., Zhang, R. Y., and Fan, J. W.: Increase of cloud droplet size with aerosol optical depth: An observation and modeling study, *J Geophys Res-Atmos*, 113, D04201, doi: 10.1029/2007jd008632, 2008.
- Zaveri, R. A., Easter, R. C., Fast, J. D., and Peters, L. K.: Model for Simulating Aerosol Interactions and Chemistry (MOSAIC), *J Geophys Res-Atmos*, 113, D13204, doi: 10.1029/2007jd008782, 2008.

759 **Table 1** Descriptions of the PM2.5 Monitoring Sites over the Houston area from TCEQ

Abbreviation	Site Descriptions	Latitude	Longitude
HA	Houston Aldine	29.901	-95.326
HDP	Houston Deer Park 2	29.670	-95.129
SFP	Seabrook Friendship Park	29.583	-95.016
CR	Conroe Relocated	30.350	-95.425
KW	Kingwood	30.058	-95.190
CT	Clinton	29.734	-95.258
PP	Park Place	29.686	-95.294
GS	Galveston 99th Street	29.254	-94.861

760

761

762

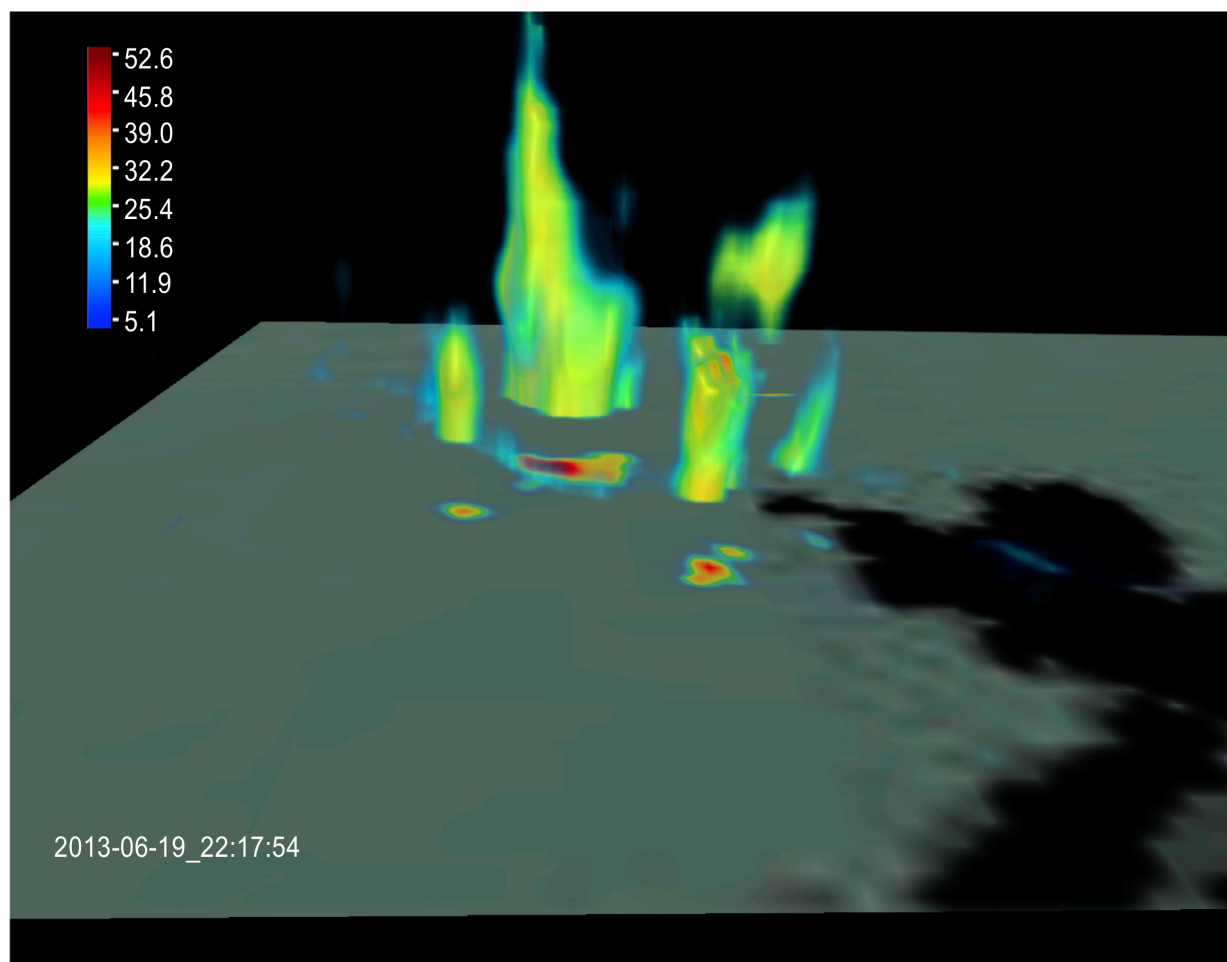


Figure 1 3D structure snapshot of radar reflectivity (unit: dBZ) from NEXRAD, overlaid with the composite reflectivity shown on the surface at the time when the maximum reflectivity is observed (2217 UTC). The dark shade shows the water body and the largest cell is in Houston.

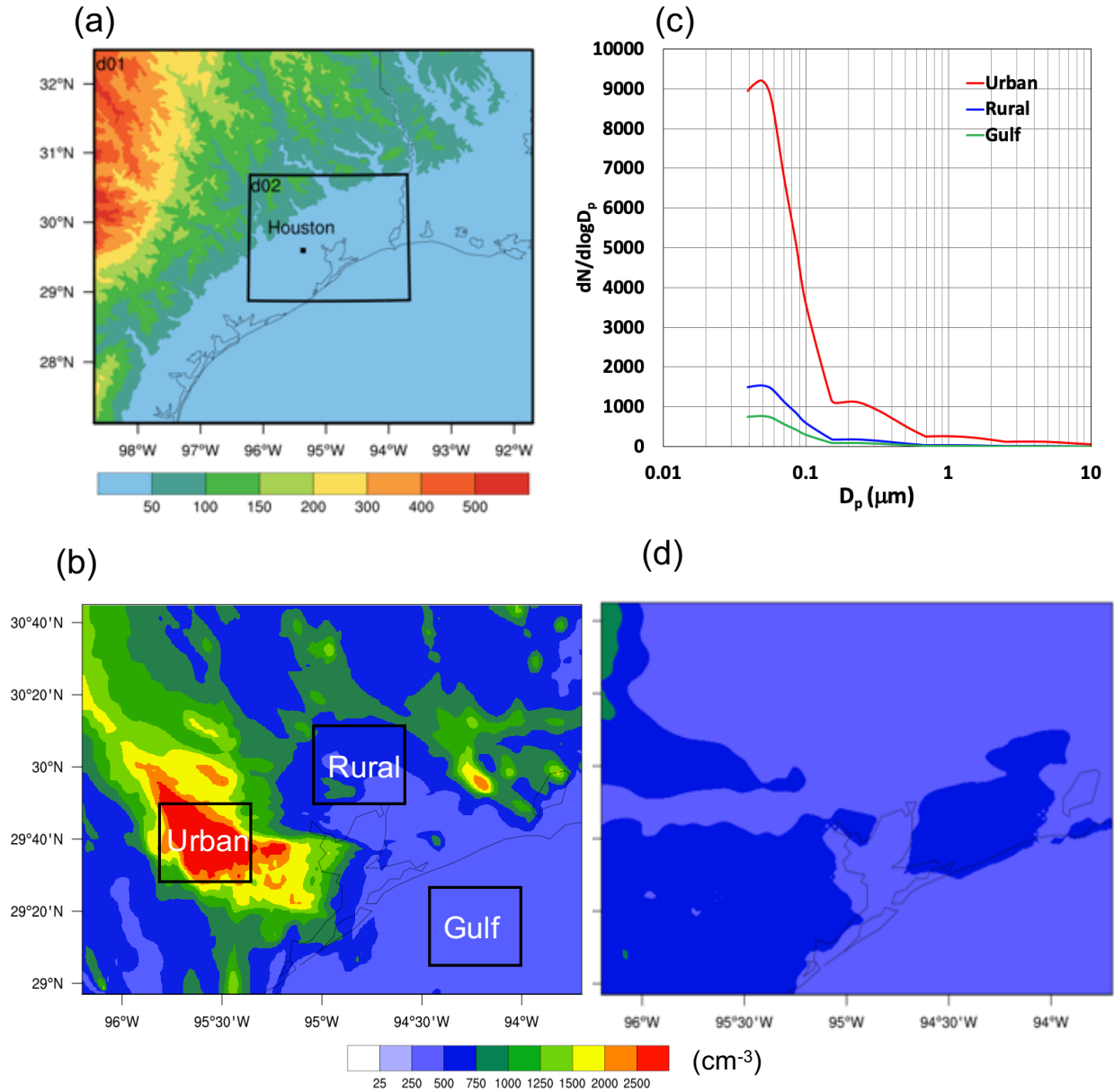


Figure 2 (a) Simulation domains with the terrain heights (unit: m), (b) aerosol number concentration (unit: cm^{-3}) from D1_MOR_anth, (c) aerosol size distributions over the urban, rural, and Gulf of Mexico as marked by three black boxes in Fig. 2b at 1200 UTC, 19 Jun 2013 (6-hr before the convection initiation), and (d) the same as Fig. 2b, but for D1_MOR_noanth in which the anthropogenic aerosols are excluded.

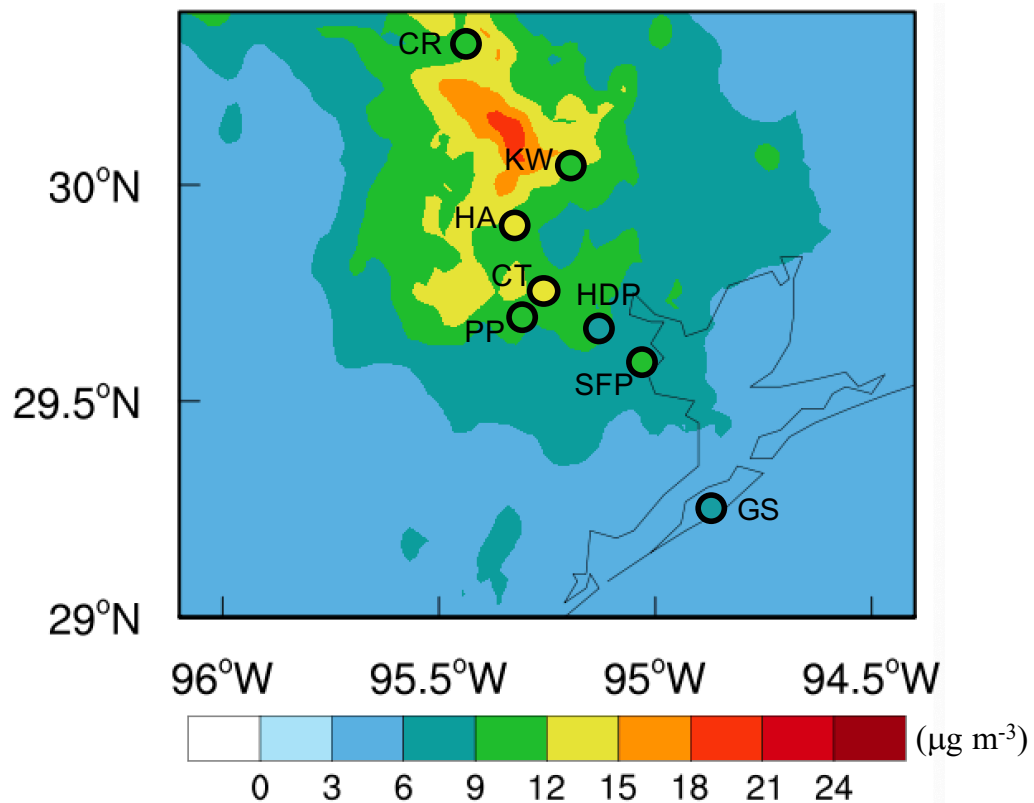


Figure 3 Comparisons of 24-hr averaged PM_{2.5} mass concentrations (unit: $\mu\text{g m}^{-3}$) between model simulation D1_MOR_anth (contoured) and site observation from TCEQ (colored circles) from 1800 UTC, 18 June 2013 to 1800 UTC, 19 June 2013 (1 day before the convection initiation). The site names and other information are shown in Table 1.

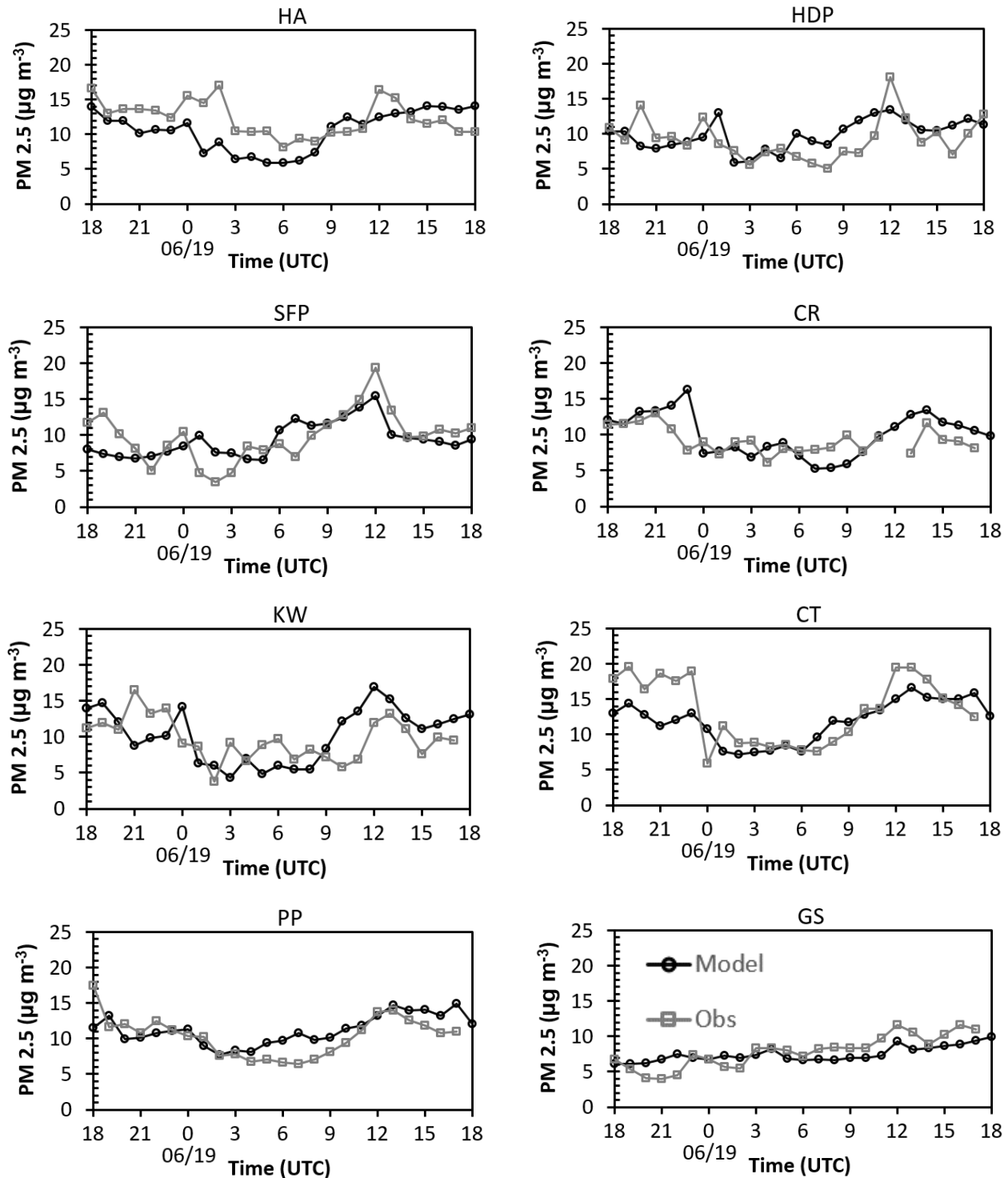


Figure 4 Site-by-site comparisons of hourly PM_{2.5} mass concentrations (unit: $\mu\text{g m}^{-3}$) from D1_MOR_anth and TCEQ site observation over 24 hours from 1800 UTC, 18 June 2013 to 1800 UTC, 19 June 2013 (1 day before the convection initiation).

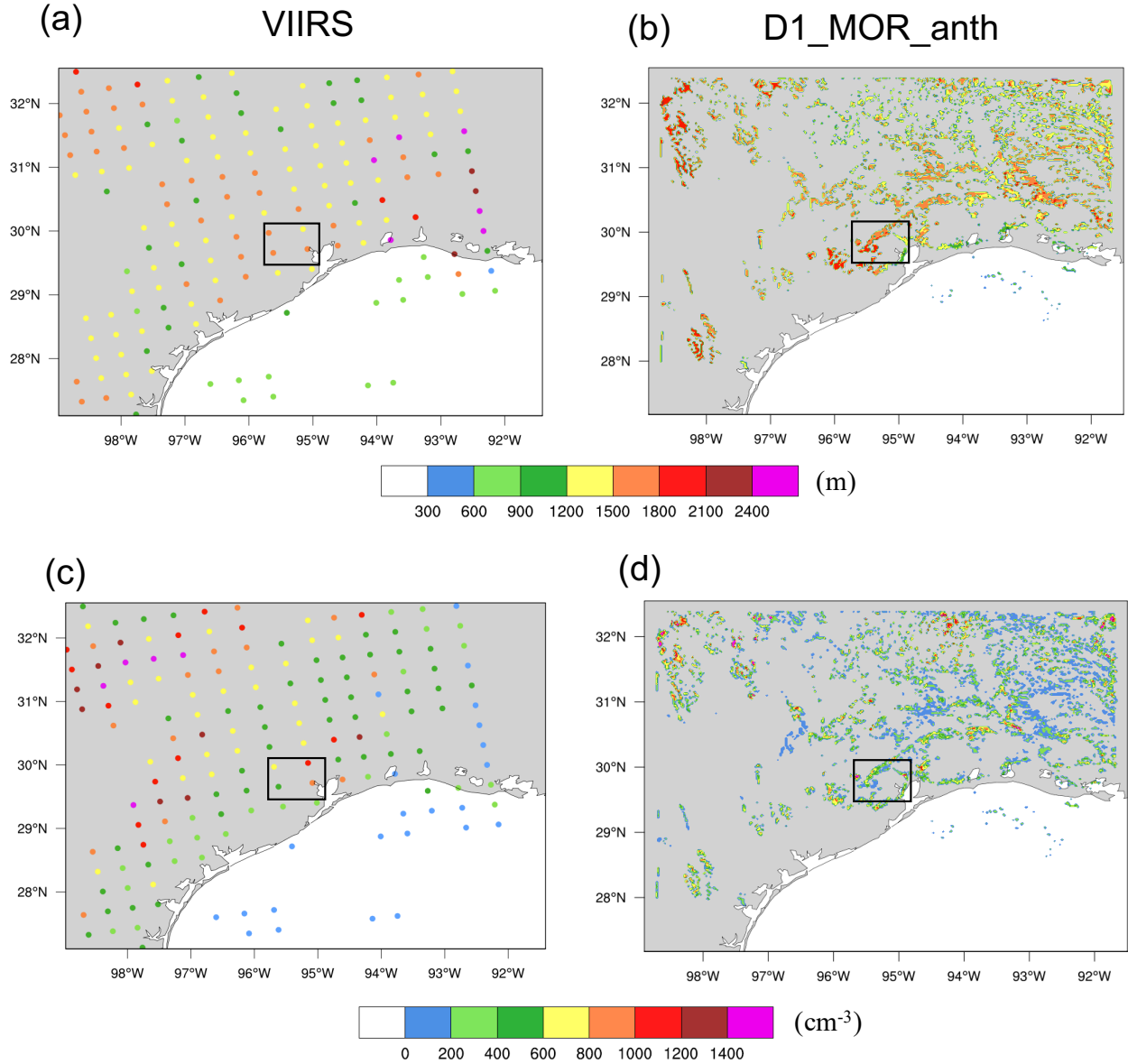


Figure 5 Evaluation of (a,b) cloud base heights (unit: m) and (c,d) CCN number concentration at cloud base (unit: cm^{-3}) from VIIRS satellite (left) retrieved at 1943 UTC (Rosenfeld et al. 2016) and model simulation D1_MOR_anth (right) at 2000 UTC, 19 June 2013. The Houston area is marked as the black box. Satellite-retrieved cloud base height was calculated from the difference between reanalysis surface air temperature (from reanalysis data) and VIIRS-measured cloud base temperature (warmest cloudy pixel) divided by the dry adiabatic lapse rate, while modeled cloud base height was determined by the lowest cloud layer with cloud mass mixing ratio greater than $10^{-5} \text{ kg kg}^{-1}$.

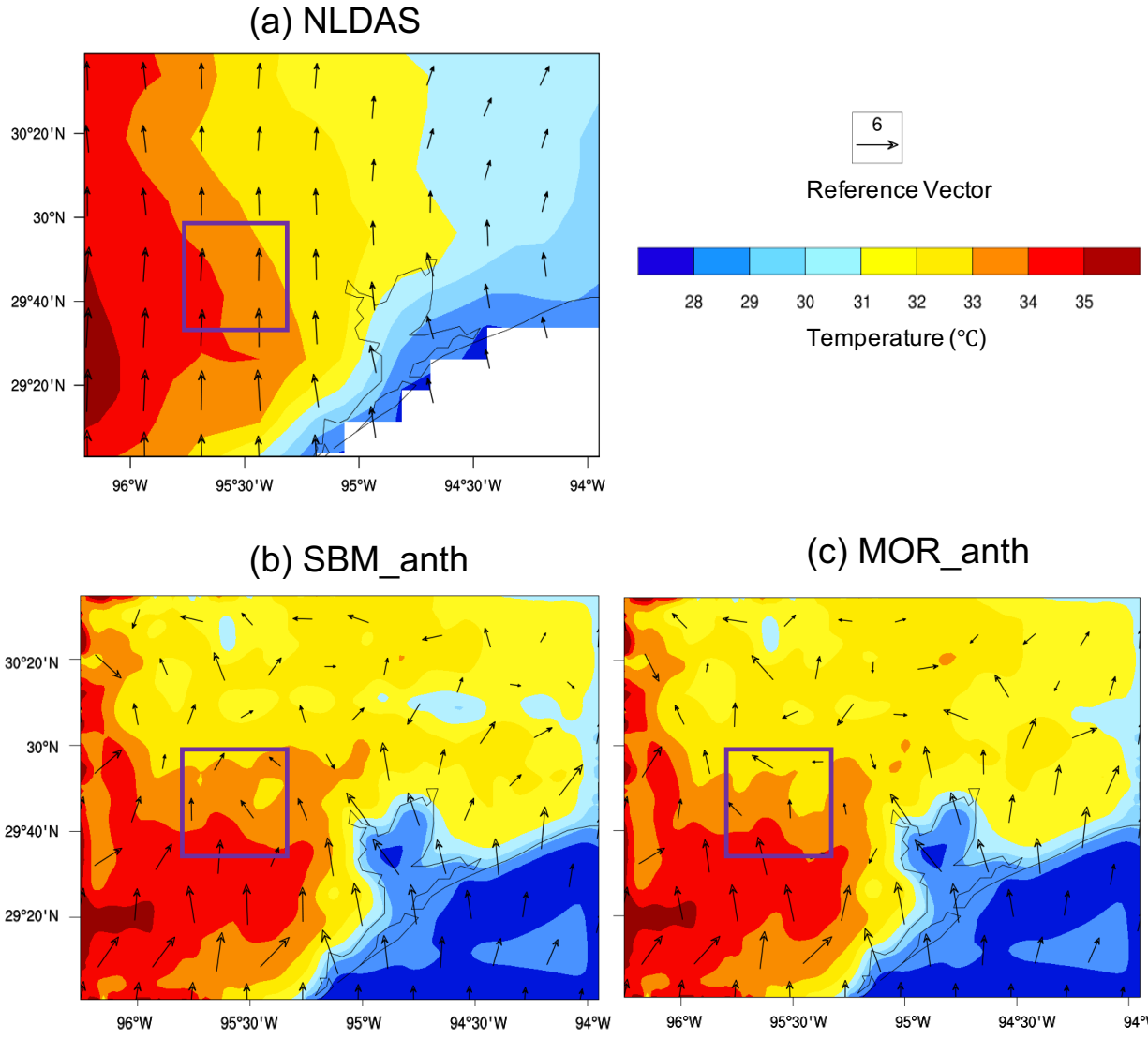


Figure 6 2-m Temperature (shaded; unit: °C) and 10-m winds (vectors; unit: m s^{-1}) from (a) NLDAS, (b) SBM_anth and (c) MOR_anth at 1800 UTC, 19 Jun 2013. The purple box denotes the Houston area.

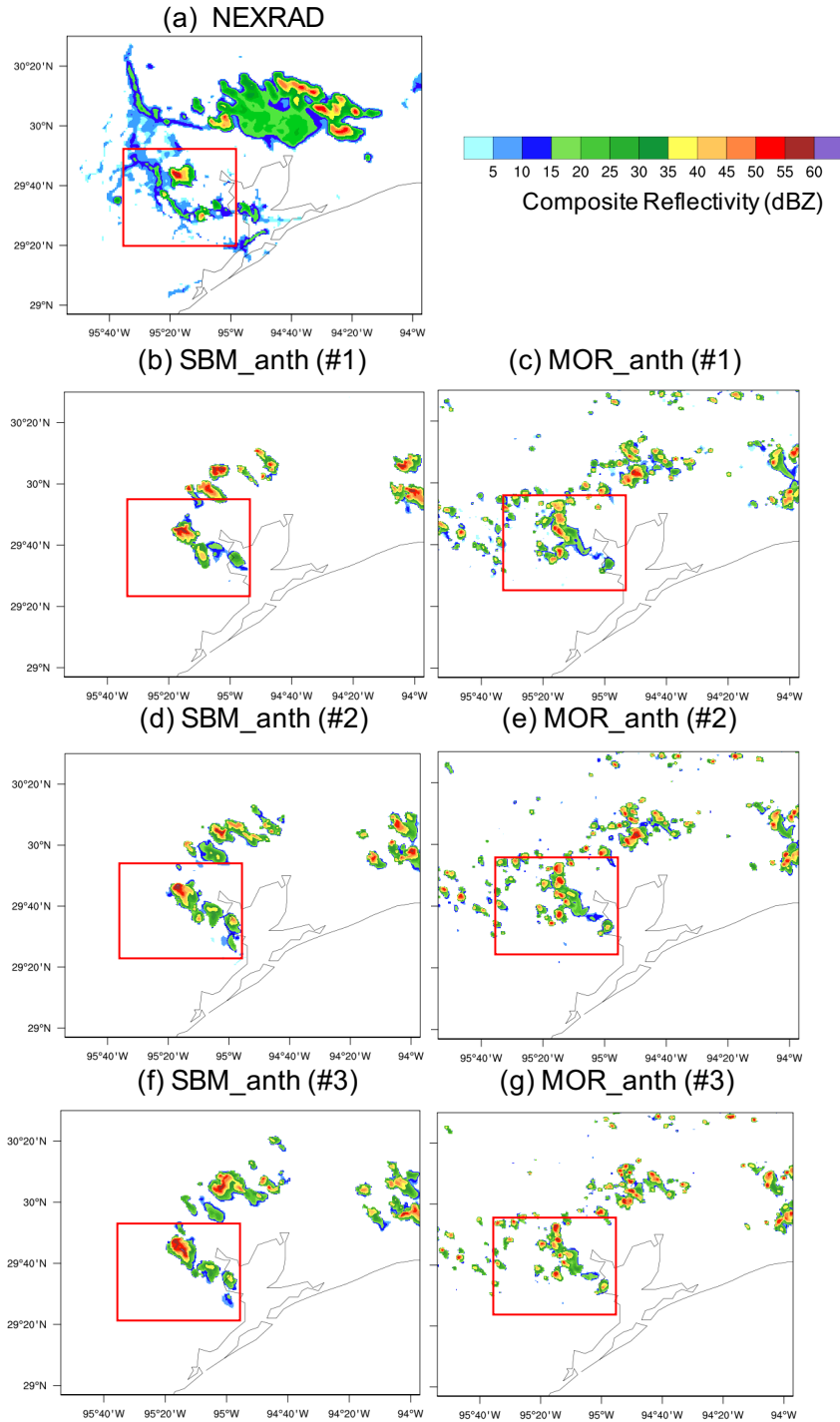


Figure 7 Composite reflectivity (unit: dBZ) from (a) NEXRAD (2217 UTC), (b, d, f) three ensemble runs for SBM_anth (2140 UTC) and (c, e, g) three ensemble runs for MOR_anth (2125 UTC) when maximum reflectivity in Houston is observed on 19 June 2013. The red box is the study area for convection cells near Houston.

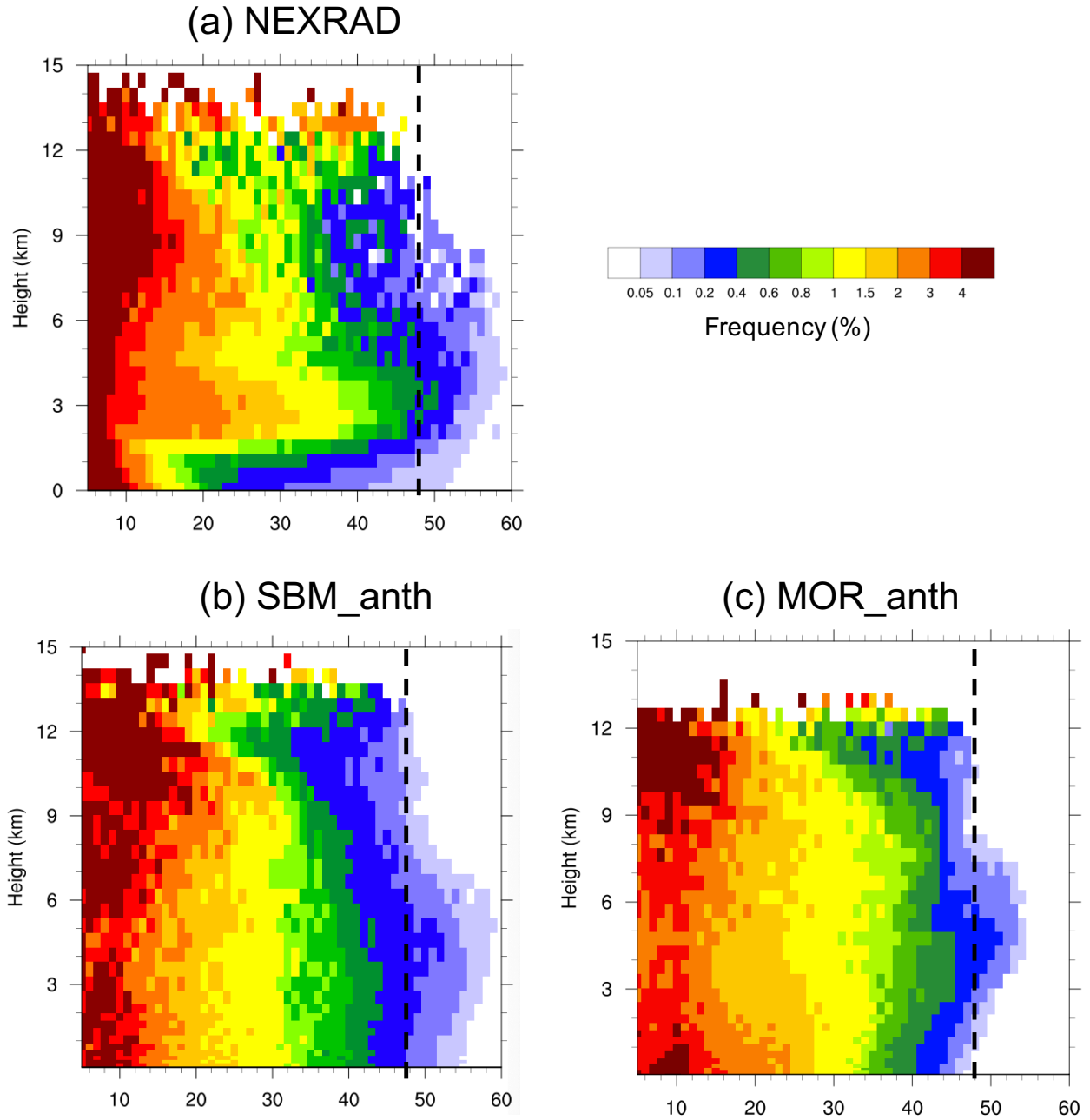


Figure 8 The CFAD of reflectivity (unit: dBZ) for the values larger than 0 dBZ from (a) NEXRAD, (b) SBM_anth and (c) MOR_anth over the study area (red box in Fig. 7) from 1800 UTC, 19 Jun to 0000 UTC, 20 Jun 2013. The black solid lines denote the reflectivity with the value of 48 dBZ. The results are the three ensemble means.

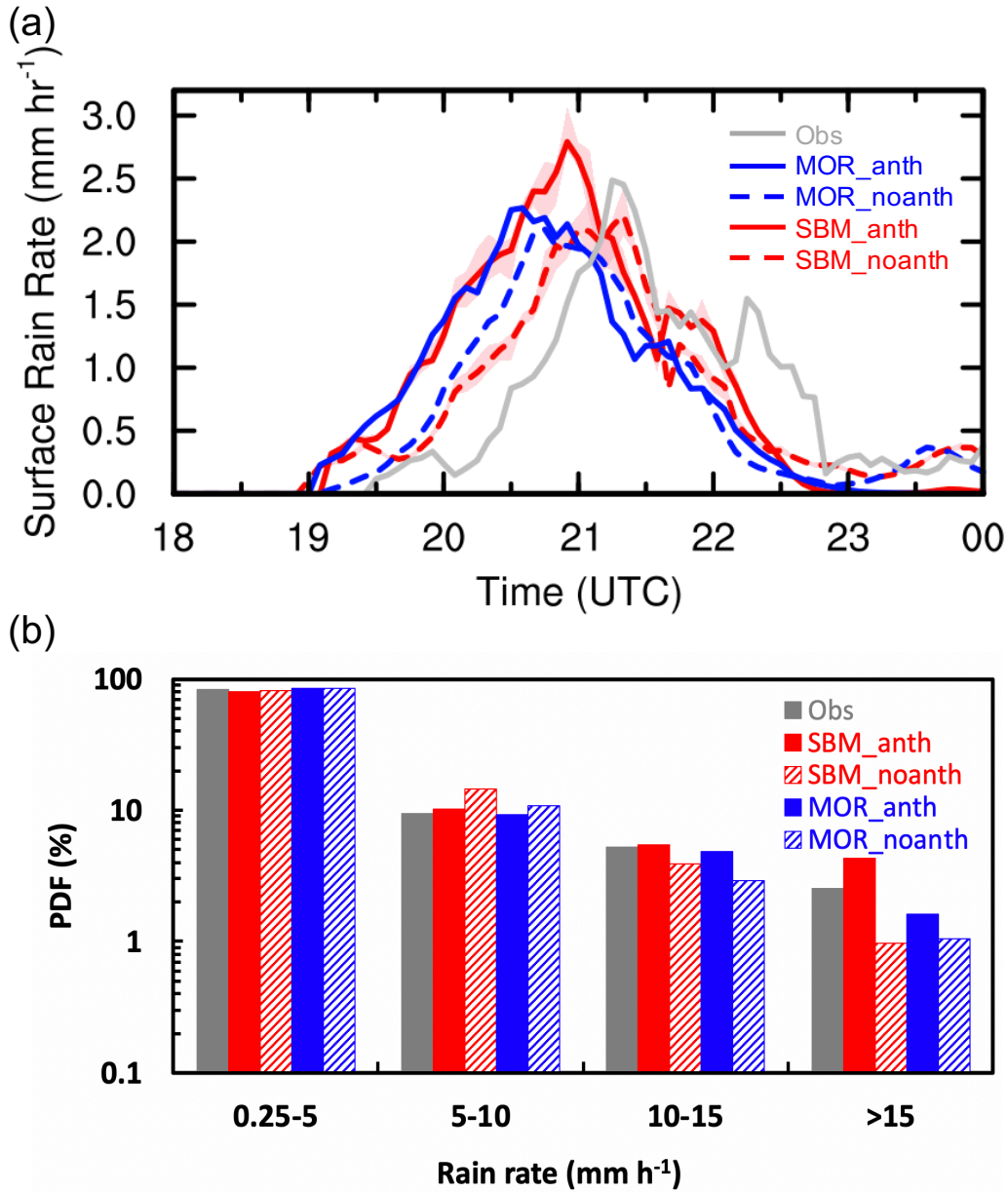
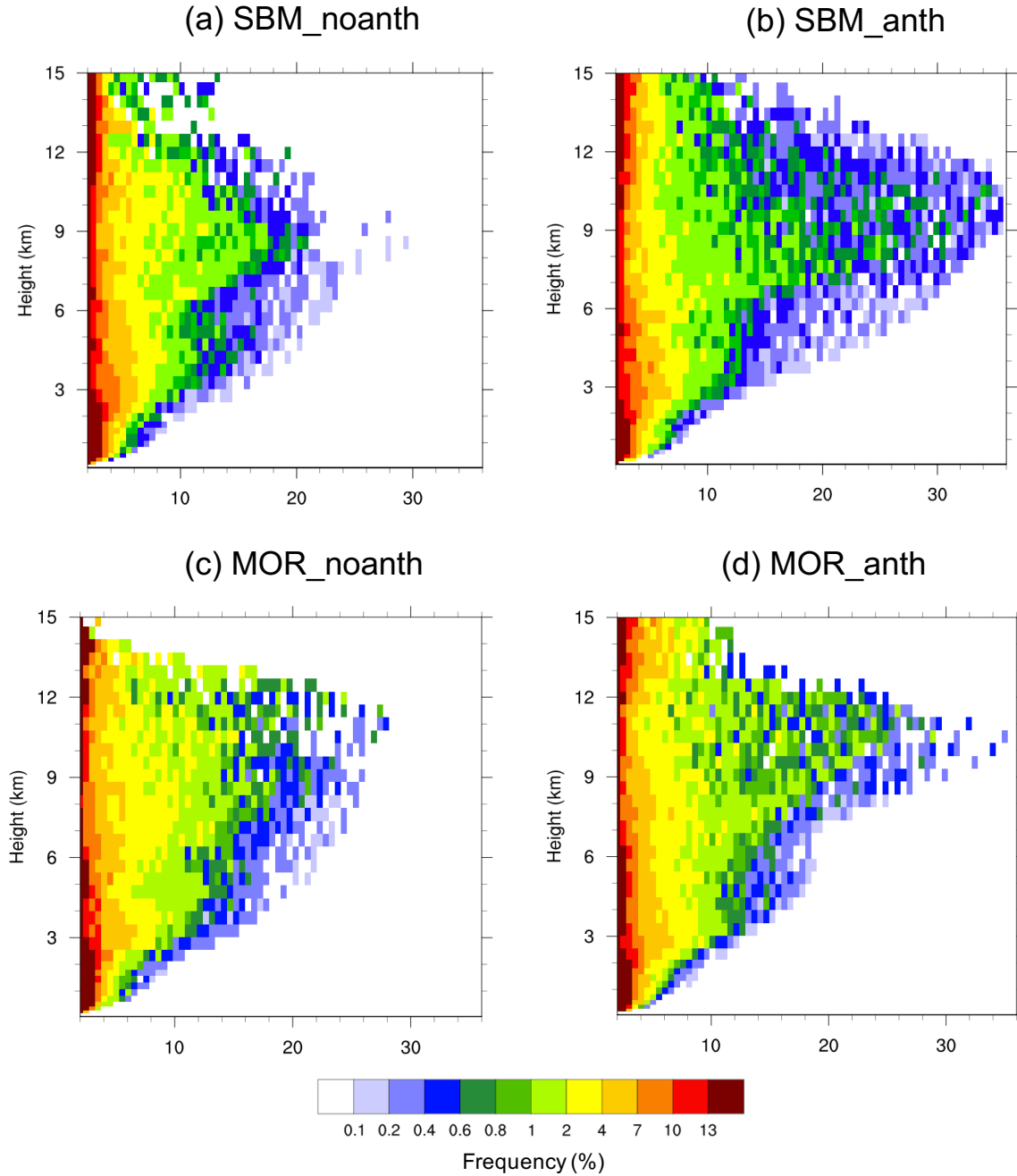


Figure 9 (a) Time series of averaged surface rain rate (unit: mm h⁻¹) and (b) PDFs of rain rate for the values larger than 0.25 mm h⁻¹ over the study area (red box in Fig. 7) from observation (grey), SBM_anth and SBM_noanth (red), MOR_anth and MOR_noanth (blue) from 1800UTC, 19 Jun 2013 to 0000 UTC, 20 Jun 2013. The observed precipitation rate is obtained by NEXRAD retrieved rain rate. Both observation and model data are in every 5-min frequency. The results are the three ensemble means. The shaded areas mark the spread of the ensemble members.



822

823 **Figure 10** CFADs of updraft velocity (unit: m s^{-1}) for values larger than 2 m s^{-1} from (a)
 824 SBM_noanth, (b) SBM_anth, (c) MOR_noanth, and (d) MOR_anth over the study area (red box
 825 in Fig. 7) during the strong convection period (2000 – 2300 UTC, 19 Jun 2013). The results are
 826 the three ensemble means.

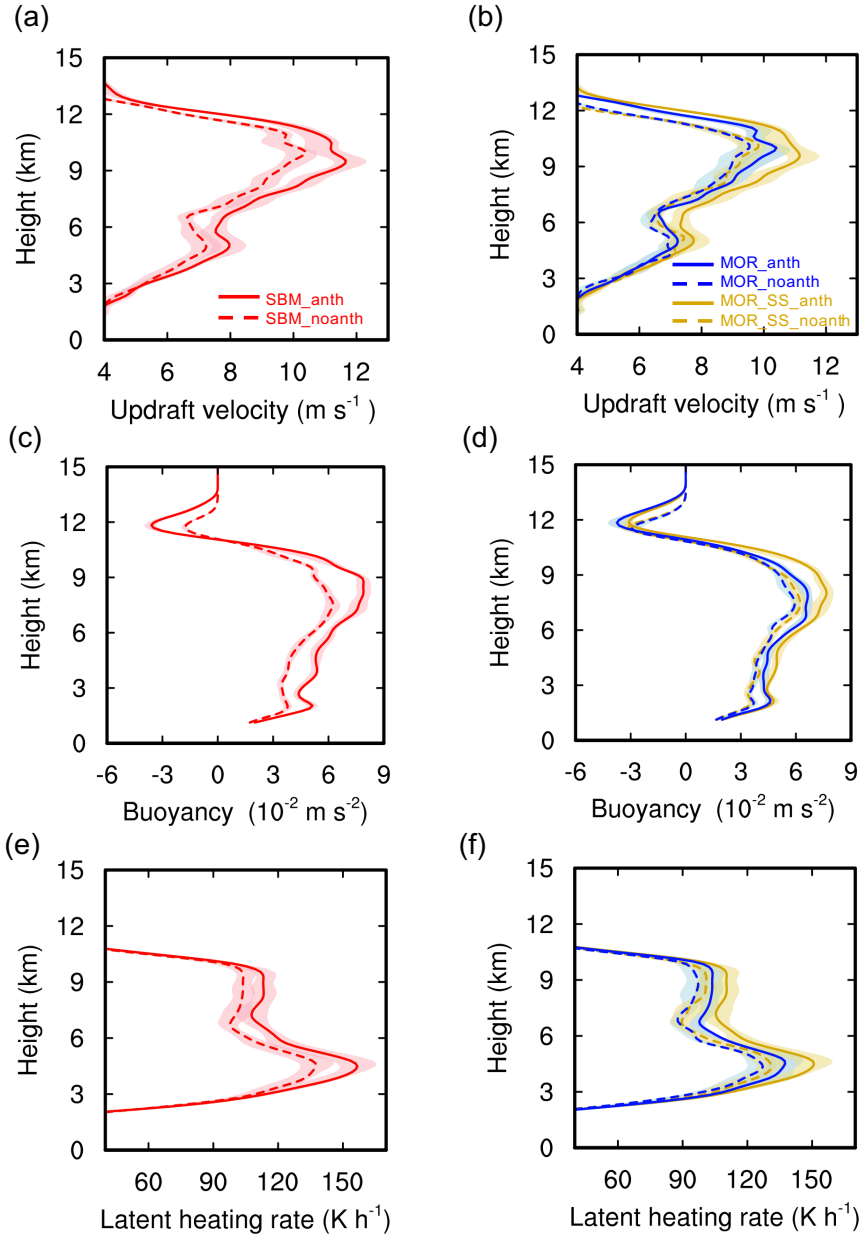


Figure 11 Vertical profiles of (a,b) updraft velocity (unit: m s^{-1}), (c,d) buoyancy (unit: m s^{-2}), and (e,f) total latent heating rate (unit: K h^{-1}) averaged over the top 25 percentiles (i.e., from 75th to 100th) of the updrafts with velocity greater than 2 m s^{-1} from the simulations SBM_anth and SBM_noanth (red), MOR_anth and MOR_noanth (blue), and MOR_SS_anth and MOR_SS_noanth (orange) over the study area (red box in Fig. 7) during the strong convection period (2000 – 2300 UTC, 19 Jun 2013). The results are the three ensemble means. The shaded areas mark the spread of the ensemble members.

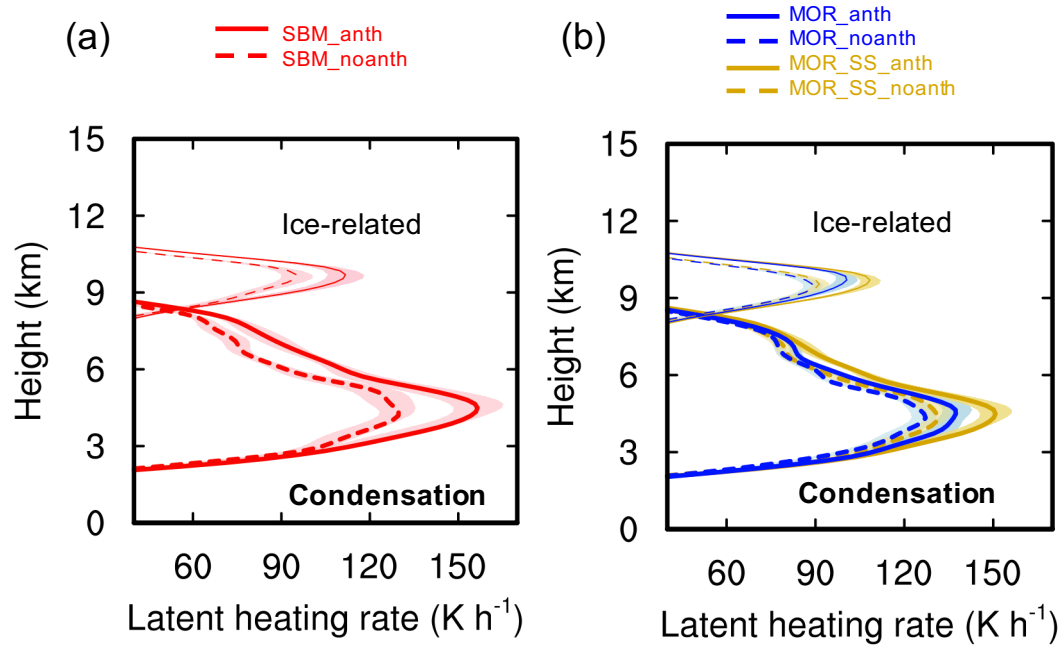


Figure 12 Vertical profiles of condensation heating rate (thick lines below 9 km; unit: K h^{-1}) and ice-related latent heating rate (thin lines above 9 km; unit: K h^{-1}) averaged over the top 25 percentiles (i.e., 75th to 100th) of the updrafts with a velocity greater than 2 m s^{-1} from the simulations (a) SBM_anth and SBM_noanth (red), and (b) MOR_anth and MOR_noanth (blue), and MOR_SS_anth and MOR_SS_noanth (orange) over the study area (red box in Fig. 7) during the strong convection period (2000 – 2300 UTC, 19 Jun 2013). Data are processed in the same way as Figure 11.

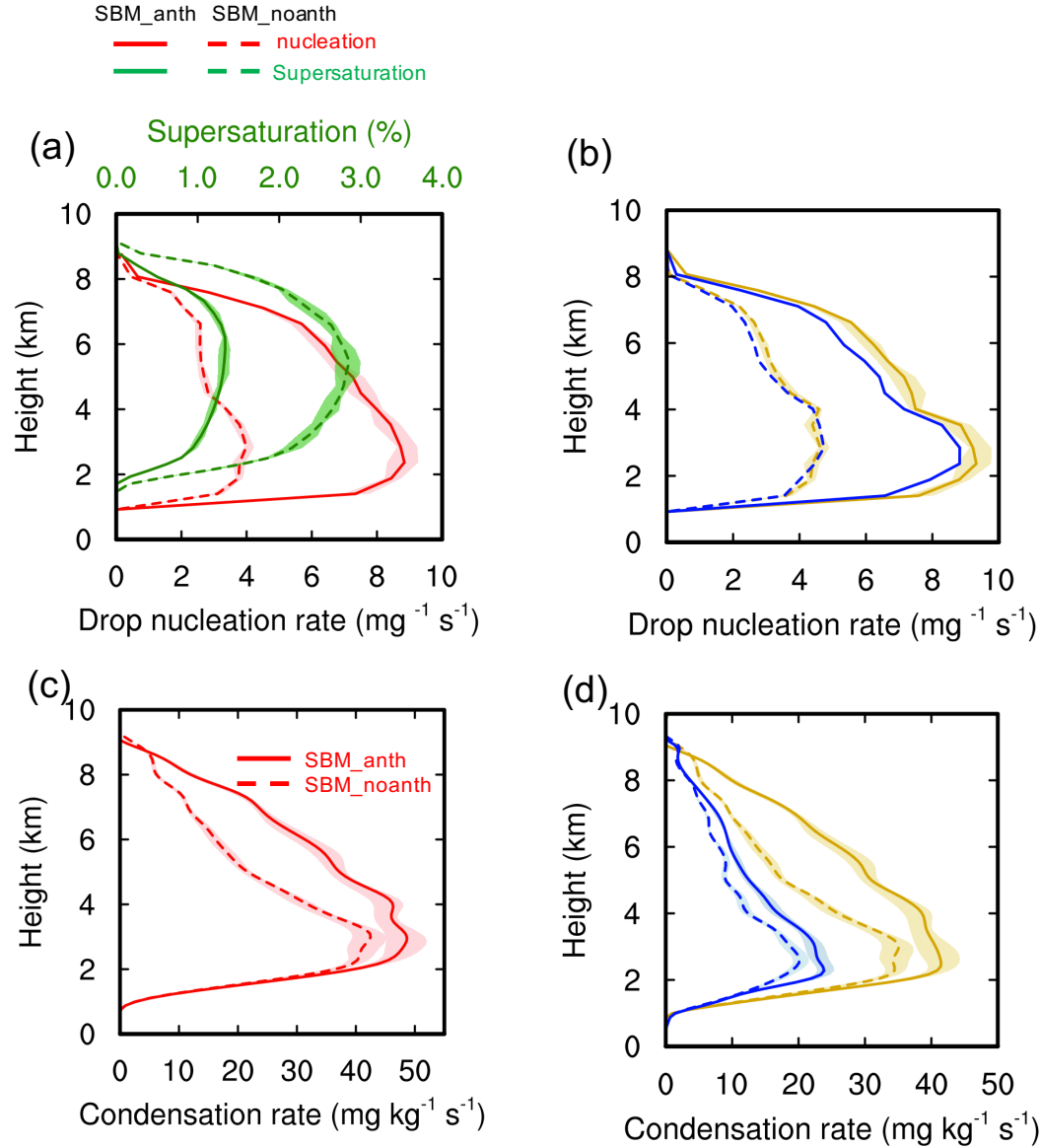


Figure 13 Vertical profiles of (a) drop nucleation rate (red; unit: $\text{mg}^{-1} \text{s}^{-1}$) and supersaturation with respect to water (green; unit: %) from SBM_anth and SBM_noanth, (b) drop nucleation rate (unit: $\text{mg}^{-1} \text{s}^{-1}$) from MOR_anth and MOR_noanth (blue), and MOR_SS_anth and MOR_SS_noanth (orange), (c) condensation rate (unit: $\text{mg kg}^{-1} \text{s}^{-1}$) from SBM_anth and SBM_noanth (red), and (d) the same as (c) but from MOR_anth and MOR_noanth (blue), and MOR_SS_anth and MOR_SS_noanth (orange), averaged over the top 25 percentiles (i.e., from 75th to 100th) of the updrafts with velocity greater than 2 m s^{-1} over the study area (red box in Fig. 7) during the strong convection period (2000 – 2300 UTC, 19 Jun 2013). Data are processed in the same way as Figure 11.

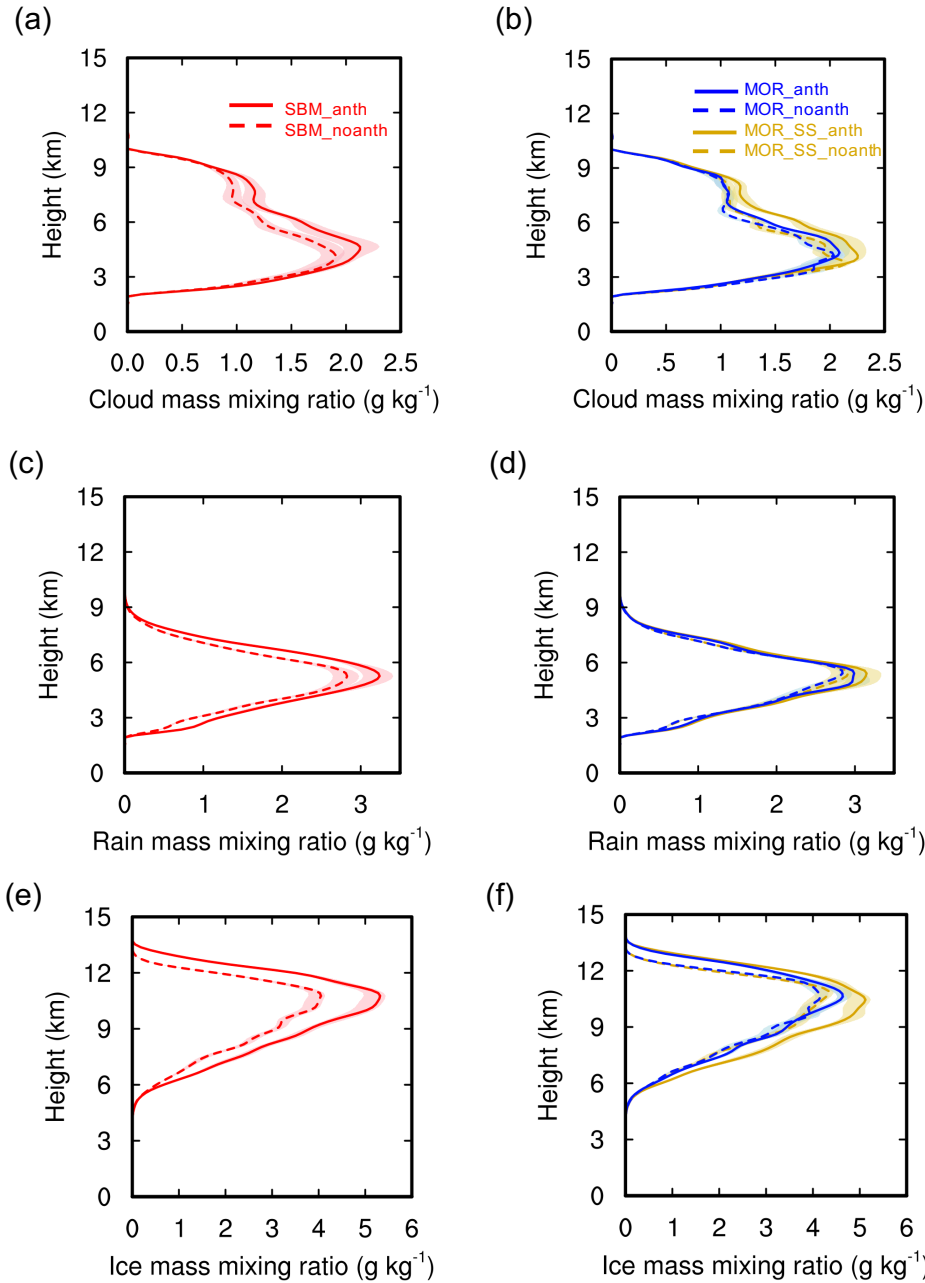


Figure 14 Vertical profiles of (a, b) cloud droplet, (c, d) raindrop and (e, f) ice particle (including ice, snow, and graupel) mass mixing ratios (unit: g kg^{-1}) averaged over the top 25 percentiles (i.e., 75th to 100th) of the updrafts with a value greater than 2 m s^{-1} from the simulations SBM_anth and SBM_noanth (red), MOR_anth and MOR_noanth (blue), and MOR_SS_anth and MOR_SS_noanth (orange) over the study area (red box in Fig. 7) during the strong convection period (2000 – 2300 UTC, 19 Jun 2013). Data are processed in the same way as Figure 11.

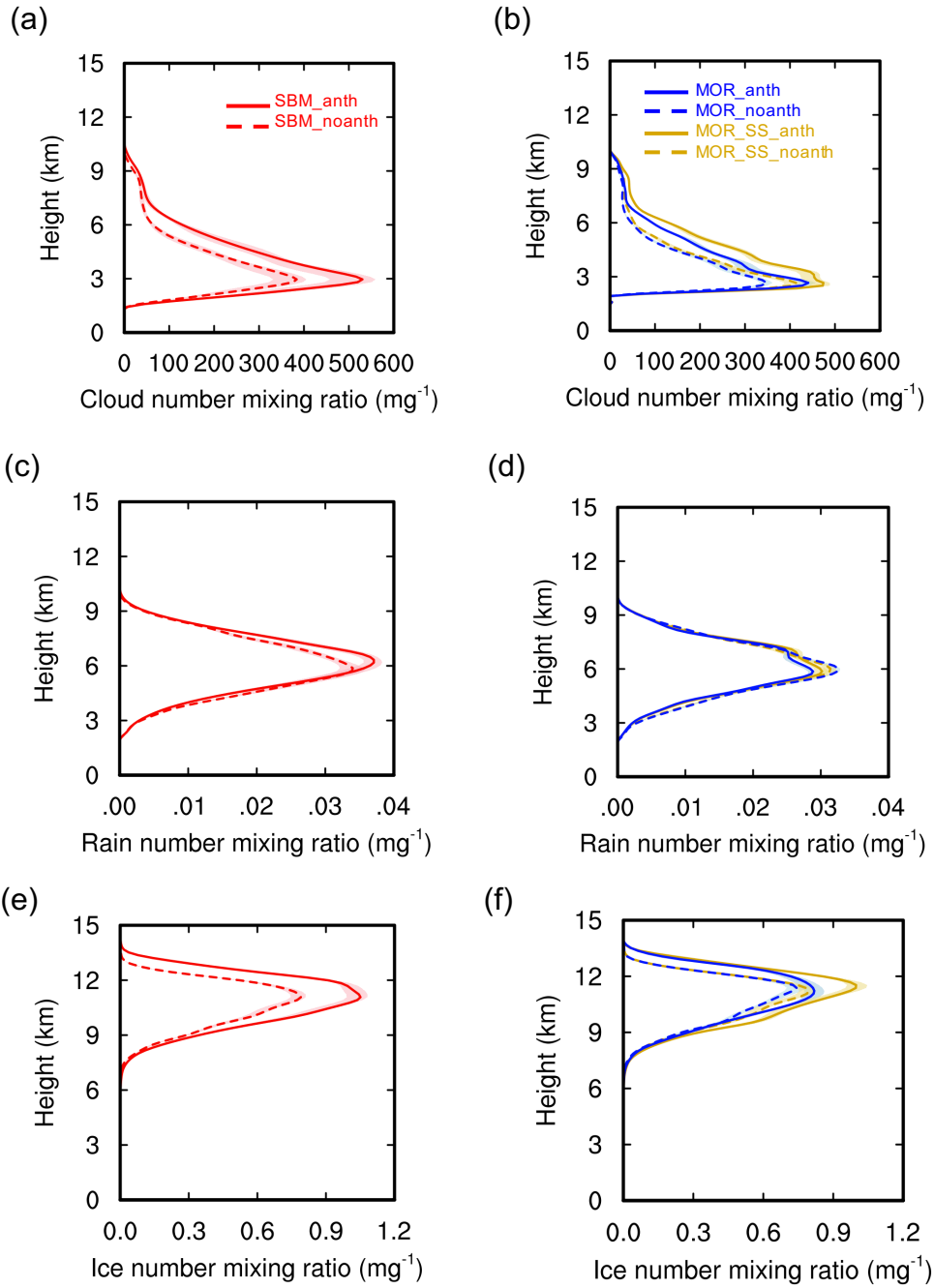


Figure 15 Same as Figure 14, but for hydrometeor number mixing ratio.